# Evidence for Holocene Earthquakes along the Húsavík-Flatey Fault in North Iceland: Implications for the Seismic Behavior of Oceanic Transform Faults

Rémi Matrau[*1], Yann Klinger[2], Thorvaldur Thorðarson[3], Esther R. Guðmundsdóttir[3], Ulas Avşar[4], Laura Parisi[1], Margherita Fittipaldi[1], and Sigurjón Jónsson[1]

## ABSTRACT

**Understanding the long-term seismic behavior of oceanic transform faults is challenging, as their location underwater generally prevents the use of classical paleoseismological techniques. The Húsavík-Flatey fault (HFF) in northern Iceland, however, is a partially emerged oceanic transform fault accommodating 6–9 mm/yr of deformation, offering a unique opportunity to apply classic inland paleoseismic methods to decipher the Holocene earthquake history of an oceanic transform fault. We excavated three fault-orthogonal paleoseismic trenches at two locations on the HFF and identified nine surface rupturing earthquakes in the last 6–8 ka. We observe little to no deformation associated with the most recent large earthquakes of 1872 (M ∼ 6.5) and the penultimate earthquake in 1755 (M ∼ 7), suggesting that these earthquakes may have occurred mainly offshore, ruptured a fault strand not sampled here, or that their magnitudes may have been overestimated. From our observations, we estimate a return time of 600 ± 200 yr for the largest earthquakes on the HFF (M 7.2–7.3), and we suggest that the known historical earthquakes are likely not representative of the largest possible earthquakes on the fault. Furthermore, our observations suggest a quasi-periodic behavior and support the quasi-repeating earthquake sequences observed from instrumental earthquake catalogs on several oceanic transform faults.**

## KEY POINTS

- Investigating the Holocene deformation of an oceanic transform fault in North Iceland.
- The first paleoseismology trenches in Iceland reveal nine events in the last 6 ka with a return time of ∼600 yr.
- Our earthquake record suggests quasi-periodic behavior of the seismicity and repeated rupture sections.

**Supplemental Material**

## INTRODUCTION

Mid-oceanic ridges are usually characterized by active volcanism along the ridge axis, by extensional normal faults orthogonal to the spreading direction, and by transform faults connecting ridge segments (Wilson, 1965). Oceanic transform faults (or fracture zones) can reach lengths of several hundreds of kilometers (e.g., the 920 km long Romanche transform fault in the Atlantic ocean) and host earthquakes of magnitudes over 7 (e.g., the 2016 $M_w$ 7.1 Romanche transform fault earthquake, Hicks *et al.*, 2020). Slip rates along oceanic transform faults range from ∼14 mm/yr on ultraslow spreading ridges such as the Andrew Bain transform fault (14–16 mm/yr) at the Southwest Indian ridge (Sclater *et al.*, 2005) to ∼145 mm/yr on fast-spreading ridges such as the Garrett transform fault (145 m/yr) at the East Pacific Rise (Wendt *et al.*, 1999). On average, major earthquakes on oceanic transform faults are moderate in size given the length of the faults (typically magnitudes 6–7), strongly controlled by the thickness of the

1. Physical Science and Engineering, King Abdullah University of Science and Technology, Thuwal, Saudi Arabia, https://orcid.org/0000-0002-8850-7791 (RM); https://orcid.org/0000-0002-9430-1351 (LP); https://orcid.org/0000-0003-3849-5726 (MF); https://orcid.org/0000-0001-5378-7079 (SJ); 2. Université de Paris Cité, Institut de Physique du Globe de Paris, CNRS, Paris, France, https://orcid.org/0000-0003-2119-6391 (YK); 3. Faculty of Earth Sciences, University of Iceland, Reykjavík, Iceland, https://orcid.org/0000-0003-4011-7185 (TT); https://orcid.org/0000-0001-6987-3641 (ERG); 4. Middle East Technical University (METU), Ankara, Türkiye, https://orcid.org/0000-0002-3224-8399 (UA)

*Corresponding author: remi.matrau@kaust.edu.sa

**Cite this article as** Matrau, R., Y. Klinger, T. Thorðarson, E. R. Guðmundsdóttir, U. Avşar, L. Parisi, M. Fittipaldi, and S. Jónsson (2024). Evidence for Holocene Earthquakes along the Húsavík-Flatey Fault in North Iceland: Implications for the Seismic Behavior of Oceanic Transform Faults, *Bull. Seismol. Soc. Am.* **XX**, 1–28, doi: 10.1785/0120230119

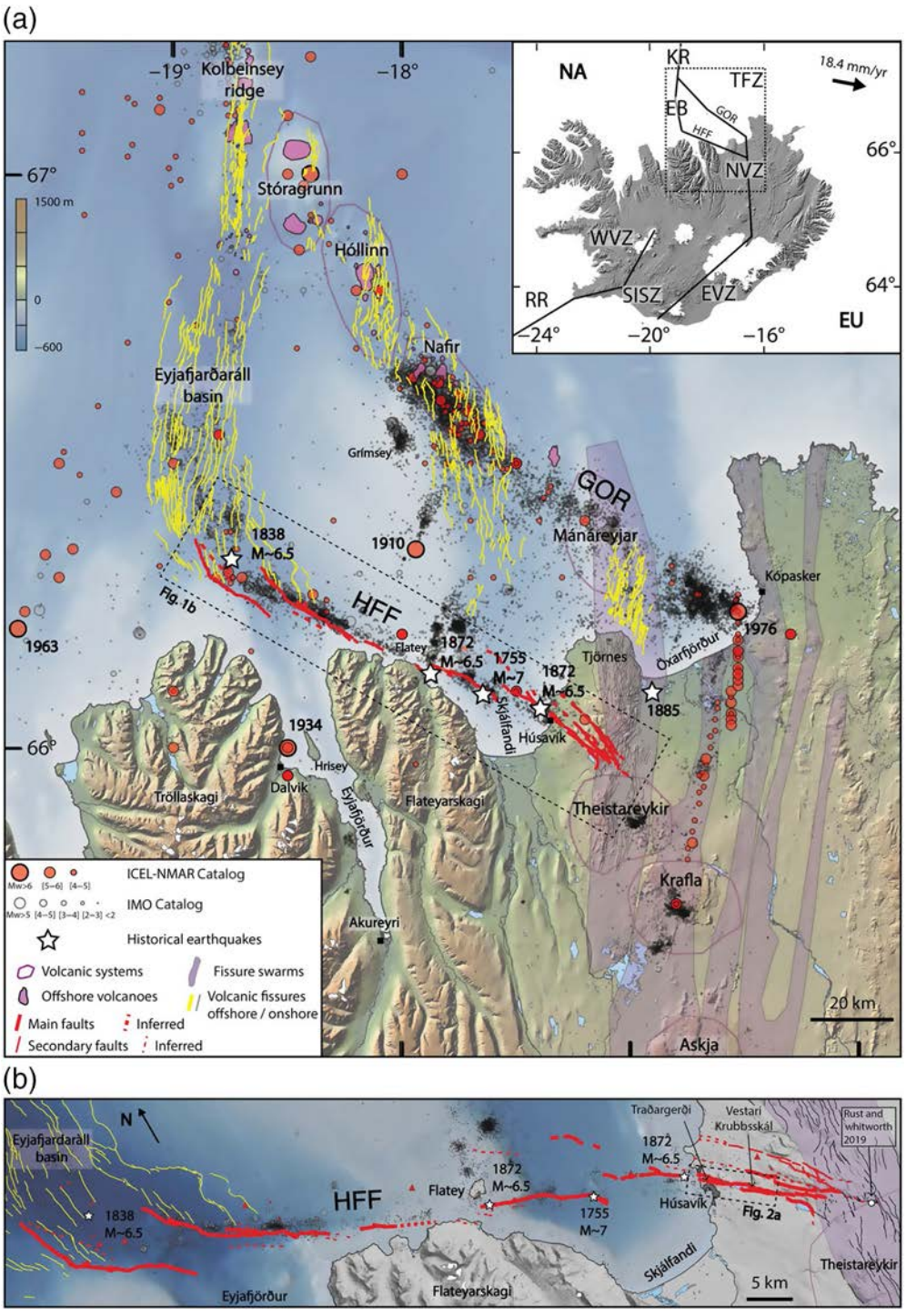


**Figure 1.** (a) Map of the Tjörnes fracture zone (TFZ) in north Iceland, with the thick red line showing the main fault traces of the Húsavík-Flatey fault (HFF), the thin red lines secondary fault traces of the HFF, and the dashed red lines inferred faults. The TFZ connects the Northern volcanic zone (NVZ) to the Kolbeinsey ridge (KR). Black circles show the instrumental seismicity from the Icelandic Meteorological Office catalog, red circles show the $M_w > 4$ earthquakes for the period 1900–2019, from the ICEL-NMAR catalog (Jóasson *et al.*, 2021), and white stars show the historical earthquakes. The dashed black frame shows the location of panel (b). The black arrow in the inset shows the spreading direction and spreading rate of Eurasia (EU) at this location with respect to North America (NA). (b) Enlargement of the HFF indicating the locations of the Traðargerði and Vestari-Krubbsskál study sites. Red lines are fault traces. Yellow and black lines are offshore and onshore volcanic fissures, respectively. EB, Eyjafjarðaráll basin; EVZ, Eastern Volcanic Zone; EU, Eurasia plate; NA, North America plate; RR, Reykjanes ridge; SISZ, South Iceland Seismic Zone; and WVZ, Western Volcanic Zone. The offshore faults have been mapped from multibeam bathymetry data, courtesy of Bryndís Brandsdóttir from the University of Iceland. The color version of this figure is available only in the electronic edition.

seismogenic zone, and itself controlled by the depth of the 600 °C isotherm (Boettcher and McGuire, 2009). The return time of these earthquakes can be short, often only a few decades (Aderhold and Abercrombie, 2016; Hicks *et al.*, 2020). Around 85% of the deformation on oceanic transform faults is estimated to be accommodated aseismically (Boettcher and Jordan, 2004) or by earthquake swarms (Roland and McGuire, 2009). Overall, the paleoseismic records of oceanic transform faults remain difficult to study because of their offshore location. Therefore, most efforts to understand the seismotectonic behavior of oceanic transform faults have focused on statistical analysis of instrumental earthquake catalogs (Boettcher and Jordan, 2004; Boettcher and McGuire, 2009; Kagan *et al.*, 2010), earthquake source inversions (Sykes and Ekstrom, 2012; Hicks *et al.*, 2020), or thermomechanical modeling (Roland *et al.*, 2010; Liu *et al.*, 2012).

The Mid-Atlantic ridge is classified as a slow-spreading ridge. Modeling and interpretation of magnetic anomalies along the Kolbeinsey ridge, north of Iceland (Fig. 1), yield spreading rates ranging from 15 to 20 mm/yr (Vogt *et al.*, 1980; Mosar *et al.*, 2002). The Tjörnes fracture zone (TFZ) in northern Iceland is a transform zone of the Mid-Atlantic ridge, connecting the offshore Kolbeinsey ridge to the onshore Northern volcanic zone (NVZ; Fig. 1). The TFZ accommodates about 18.1 ± 0.4 mm/yr of oceanic spreading between the North American plate and the Eurasian plate (MORVEL,

DeMets *et al.*, 2010). The deformation is accommodated by two main fault zones: the Grímsey oblique rift (GOR) to the north and the Húsavík-Flatey fault (HFF) to the south (Fig. 1). Although the historical record is limited in this area, 8–9 moderate-to-large earthquakes (M 6–7) have been reported in the TFZ in the past 270 years (Fig. 1), of which three to four might have occurred on the HFF (Stefánsson *et al.*, 2008; Thorgeirsson, 2011). The TFZ is almost entirely located offshore, except for a 20 km long onshore section of the HFF, from the town of Húsavík to the junction with the NVZ (Fig. 1b). This on-land section, therefore, provides a unique opportunity to investigate in detail the history of past earthquakes along the HFF. Determining the size and frequency of moderate-to-large earthquakes is essential to understand how the deformation is accommodated across the TFZ and in general along transform faults.

Indeed, the long-term behavior of fracture zones and oceanic transform faults, at the scale of multiple seismic cycles, remains difficult to assess, simply because oceanic transform faults lie at the bottom of the ocean. We propose here to use the peculiarity of the TFZ in northern Iceland to bring a new perspective on oceanic transform faults using paleoseismological methods. To study the occurrence of the past earthquakes along the HFF, we excavated 11 paleoseismic trenches and several pits at two locations 5.5 km apart: four in Vestari-Krubbsskál 5 km southeast of Húsavík and seven in Traðargerði just north of Húsavík (Figs. 1, 2). Five trenches were dug orthogonal to the fault to investigate the timing of the earthquakes. Six additional trenches were dug parallel to the fault, which are not discussed in detail here, to investigate the slip rate of the fault and to characterize coseismic displacement associated with the past earthquakes.

Hence, the focus of this study is to build a catalog of earthquakes for the HFF by determining the timing of the past earthquakes along the onland section of the HFF. To constrain the timing of the events, we took advantage of the specific volcanic environment of Iceland to combine radiocarbon ages with the well-documented regional tephra sequence. In the following, we first summarize the specific characteristic of the local seismotectonics context in North Iceland. Then, we describe the trench sites of Traðargerði and Vestari-Krubbsskál and their paleoseismological records. Finally, combining the observations from the two sites together with the different age constraints, we build the most complete catalog to date of moderate-to-large earthquakes on the HFF during the Holocene, providing insights on the seismic cycle along the HFF, which we compare with other oceanic transform faults.

## SEISMOTECTONIC SETTING

In Iceland, the Mid-Atlantic ridge is offset eastward with the offset between ridge segments accommodated by two transform zones, the South Iceland seismic zone to the south, and the TFZ to the north (Fig. 1). Over time, the onshore spreading axis is stepping eastward to maintain its location relative to the underlying mantle plume (Sæmundsson, 1974; Garcia *et al.*, 2003; Sæmundsson, 2013; Karson, 2017).

The analysis of magnetic polarities, stratigraphic sequences, and stratigraphy of basalts suggest that the jump from the old rift axis following the Skagi peninsula just west of Tröllaskagi to the present-day rift axis in Öxarfjörður (Fig. 1) occurred 4–8 Ma ago (Sæmundsson, 1974). More recently, Argon–Argon radiometric dating of dykes in northern Iceland has shown that the activity of the present-day rift started 8–8.5 Ma ago, whereas the activity of the older rift only stopped around 3 Ma ago, suggesting that the two rift zones remained simultaneously active for 5–5.5 Ma (Garcia *et al.*, 2003). In addition, stratigraphic observations of Miocene basalts and interglacial lava flow in the vicinity of the HFF suggest that the fault has been active for at least 5 Ma (Sæmundsson, 1974; Sæmundsson and Karson, 2006). However, numerical modeling of stress orientations combining present-day maximum stresses from earthquake focal mechanism solutions with paleostresses derived from dike and fracture orientations suggest that the activation of the HFF is related to the initiation of the TFZ (Homberg *et al.*, 2010) and therefore of similar age as the TFZ around 8–8.5 Ma (Garcia *et al.*, 2003). This inference is also supported by modeling of fault interactions and slip distribution along faults of the TFZ, showing that in most cases only one fault is active at a given time (Homberg *et al.*, 2010). Observations show that rifts are usually propagating away from plumes, creating so-called pseudofaults at the edges of the propagating tip of the rift (Hey, 2005; Karson, 2017). Structural observations and analysis of the geometry of these pseudofaults suggest that the NVZ is propagating northward into Öxarfjörður (Sæmundsson, 2013; Karson, 2017), consequently decreasing the slip rate of the HFF from ~10 mm/yr to few millimeters per year over the last 1 Ma, as the GOR becomes the main active structure (Sæmundsson, 2013).

The TFZ is a complex oceanic transform zone where deformation occurs mainly on two lineaments: the GOR to the north, which is formed by a set of en echelon, left-stepping, north–south-oriented, basins and four volcanic systems (Magnúsdóttir *et al.*, 2015) and the HFF to the south, a right-lateral, transtensional, transform fault system. The GOR is located entirely offshore and is volcanically active (Gudmundsson, 2000) with two known historical eruptions in 1372 and in 1867–1868, the later accompanied by an earthquake of estimated magnitude M 6 (Magnúsdóttir and Brandsdóttir, 2011). The GOR is seismically very active and currently accounts for ~60% of the earthquakes in the TFZ (Jónsdóttir *et al.*, 2019). Two significant instrumental earthquakes are known to have occurred within the GOR: the M ~7 earthquake in 1910 located somewhere close to Grímsey island and the M 6.2 earthquake in 1976 located in Öxarfjörður just offshore of Kópasker village (Fig. 1) at the tip of the Krafla fissure swarm that may have resulted from the onset of the Krafla rifting episode in 1975–1984. Modeling

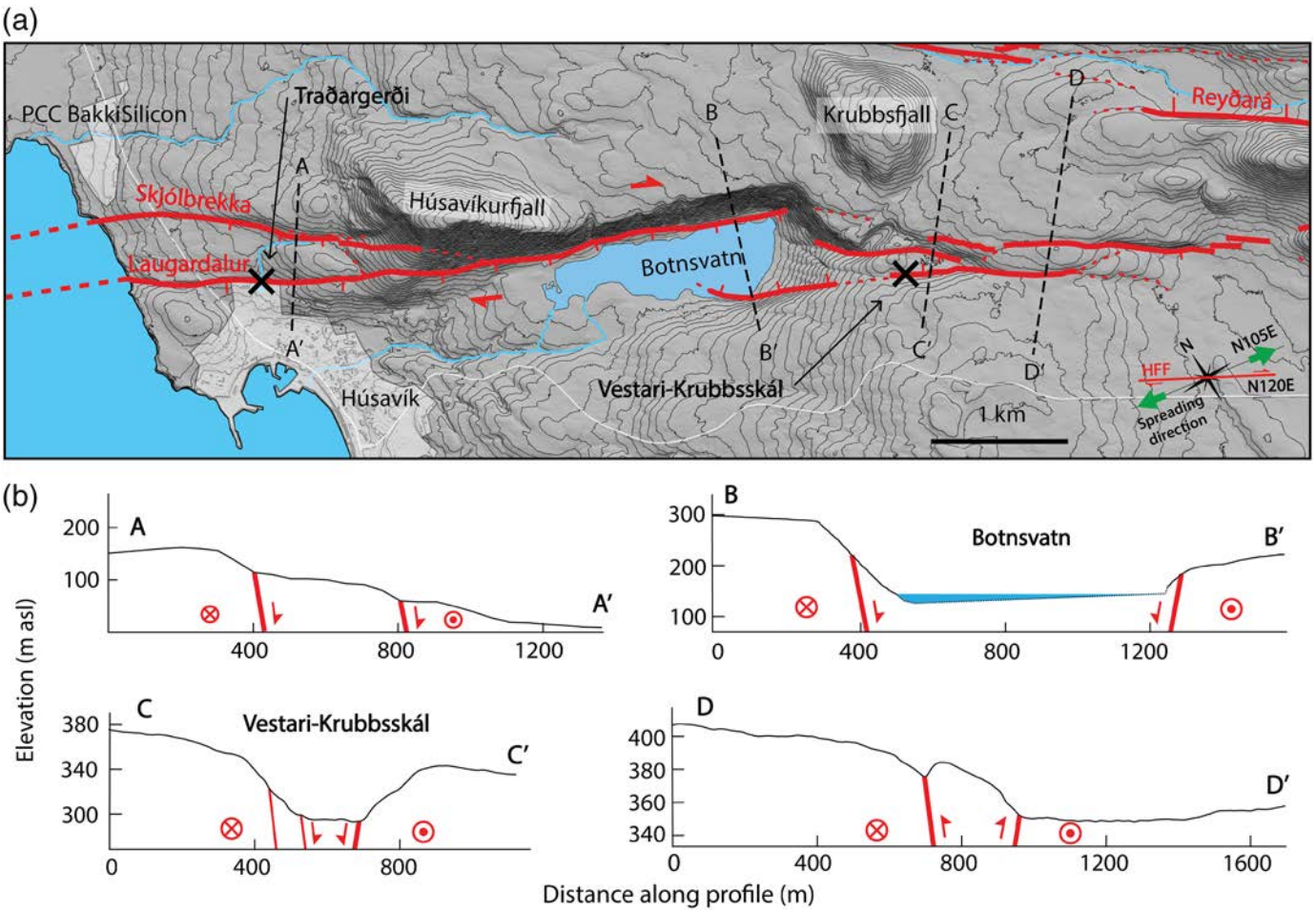


**Figure 2.** (a) Fault map of the western half of the onshore sections of the HFF (HFF) overlaid on a 2 m light detection and ranging digital elevation model from the Land Survey of Iceland. The red lines show the main fault strands, whereas red dotted lines show inferred faults. The dashed black lines locate the topographic profiles shown in panel (b), and the black crosses show the locations of the two trench sites. (b) Fault-orthogonal topographic profiles at four locations: north of Húsavík (AA′), across Botnsvatn lake (BB′), in Vestari-Krubbsskál (CC′), and in a small restraining bend (DD′) with vertical exaggeration of 1.4, 1.4, 6.2, and 4.6, respectively. The fault geometries at depth are only inferred not measured. The color version of this figure is available only in the electronic edition.

of geodetic data suggests that half to two-thirds of the motion (9–12 mm/yr) of the TFZ is currently accommodated by the GOR (Metzger and Jónsson, 2014).

The HFF is 100 km long, mainly located offshore. It extends from the Eyjafjarðaráll basin to the west, representing the southern continuation of the Kolbeinsey ridge, to the Theistareykir fissure swarm to the east, which is the westernmost active volcanic system of the NVZ (Fig. 1). The HFF cuts across Eyjafjörður and the Skjálfandi bay, and runs through the town of Húsavík on the western shore of the Tjörnes peninsula. The HFF strikes on average ~N110°E along the offshore sections. The HFF includes two main offshore left-stepping relay zones (Fig. 1): one in the middle of the Skjálfandi bay and another one between Flatey island and Flateyjarskagi (Magnúsdóttir *et al.*, 2015), resulting in two local compressional jogs. The fault section onshore is about 20 km long, extending from the coastal town of Húsavík to the junction with the Theistareykir Fissure Swarm (Figs. 1, 2). The onshore segments of the HFF strike between ~N120°E and ~N130°E on average and up to N140°E close to the Theistareykir Fissure Swarm. In northern Iceland, the average plate motion direction is ~N105°E, implying significant obliquity between the strike of the HFF onshore and the spreading direction. The HFF is a subvertical strike-slip fault (Sæmundsson and Karson, 2006) with several relay zones along the fault onland, both compressional and extensional (Fig. 2).

North of Húsavík, the fault consists of two subparallel branches: Laugardalur to the south, where our site of Traðargerði is located, and Skjólbrekka to the north (Sæmundsson and Karson, 2006). These two branches are 300–550 m apart (Fig. 2). From the east, these two branches splay off the main fault trace on the southern slope of Húsavíkurfjall, the Húsavík mountain (Fig. 2) and then run subparallel for ~3.5 km before continuing offshore in the Skjálfandi bay. The height of the scarp for the Skjólbrekka fault strand varies significantly along strike from ~60 m to the east

down to ~3 m to the west. The scarp of the Laugardalur fault strand is a low-angle fault scarp, 30–40 m high (profile AA′ in Fig. 2). Along Húsavíkurfjall, an 800 m right step in the fault system results in a pull apart basin where Botnsvatn lake is located (topographic profile BB′ in Fig. 2). Just east of the Botnsvatn basin, the geometry of secondary faults is responsible for a smaller pull-apart basin: the Vestari-Krubbsskál basin, (topographic profile CC′ in Fig. 2). From Vestari-Krubbsskál eastward, several left steps in the faults result in local pressure ridges that are 600–1500 m long and up to 60 m height (the western most pressure ridge shown in topographic profile DD′ in Fig. 2). The fault then lies at the base of a south facing slopes and finally connects to the Theistareykir fissure swarm in a set of en echelon left-stepping faults and fissures (Gudmundsson *et al.*, 1993; Pasquare Mariotto *et al.*, 2015; Tibaldi *et al.*, 2016). North of the HFF, another fault section, sometimes referred to as the Reyðará fault (Fig. 2), runs subparallel to the HFF. It is not clear if the Reyðará fault was active during the Holocene.

The HFF is a seismically active structure that has hosted several energetic seismic swarms at its western end in the past three decades with earthquakes of magnitude up to 5.7 (Passarelli *et al.*, 2018). Maccaferri *et al.* (2013) reported much lower seismicity rate eastward of Flatey island in the Skjálfandi bay and along the onshore section of the fault system. Such reduced seismic activity on the eastern section of the fault is likely due to the stress shadow induced by the Krafla rifting episode in 1975–1984 (Maccaferri *et al.*, 2013). Historical information about significant earthquakes in northern Iceland is limited before the eighteenth century, and prehistorical accounts are almost nonexistent. The most significant earthquakes on the HFF (Fig. 1) in the last 300 yr occurred in 1755, 1838, and during a double event in 1872 (Stefánsson *et al.*, 2008; Thorgeirsson, 2011).

## TRAÐARGERÐI

### Traðargerði morphology

Traðargerði is located just north of Húsavík in horse stables at an elevation of ~55 m (Figs. 2, 3). The main geological unit is a Pleistocene tillite (Waltl *et al.*, 2018). We acquired 200 aerial photographs using an Unmanned Aerial Vehicle (UAV) to map the structures of Traðargerði and to compute orthomosaic map and digital surface model (DSM) using the structure from motion software Agisoft PhotoScan (now Agisoft Metashape). To avoid distortion, we used five ground control points achieving 3.27 cm/px and 6.55 cm/px of resolution for the orthomosaic and for the DSM, respectively.

The main morphological feature is a 50 m wide and 15 m deep incision cutting through the underlying Pleistocene tillite unit. The southern edge of the hill composed of tillite is limited by the cumulative scarp, which is about 30–40 m high. Its base is characterized by a steeper scarp of about 2–4 m high, which corresponds to the active fault trace (Fig. 3). Eroded sediments from the gully were redeposited at the outlet of the drainage where they form an 80 m long by × 80 m wide alluvial fan (Figs. 2, 3). The active river is currently flowing along the eastern edge of the fan. Some of the upper parts of the morphology have been modified by human activity, in particular, near the apex of the fan. A small bridge was built across the gully at its southern end, and a water tank was buried downstream of the bridge. In addition, three pipes are connected to the water tank and to the active channel, and are running across the alluvial fan. Finally, an irrigation channel, currently backfilled, was excavated north of the fan, part of which was visible in the trench. Water seeps out along a 3–4 m high × ~40 m long scarp located just west of the fan. This seepage could be related either to water leaking from an aquifer located just north of the fault or to fluid circulation within the fault zone. The area just downstream of this scarp is currently a swamp embedded in an offset abandoned river bed (blue surface in Fig. 3b). We observe four levels of inset alluvial terraces in the gully, upstream of the fault, but none could be recognized downstream of the fault (Fig. 3). Thus, although the fault motion is dominated by strike-slip motion, the local morphology suggests that at some point vertical deformation was also accommodated. The presence of the alluvial fan and the alluvial terraces at the outlet of the ravine suggest transportation and deposition of sediments. Using both fault scarps located east and west of the gully (Fig. 3b), it is possible to project the fault location across the alluvial fan despite the fact that no topographic signature of the fault is visible on the surface of the fan. Detailed fault mapping close to the apex of the fan suggests that the fault makes a right step that is responsible for a pull-apart basin of about 6–7 m width. This basin is expressed as a flatter area in the topography at the top of the fan (see contour lines in Fig. 3d and topographic profile AA′ in Fig. 3c), probably due to the filling of the extensional depression by sediments from the gully.

We excavated seven trenches at the Traðargerði site for earthquake recognition (Fig. 3d): one across the fault trace on the western side of the alluvial fan (Tr1, which is 35 m long, 2 m wide, and 2.5 m deep), one parallel to the fault trace just north of the alluvial fan (Tr4, which is 23 m long, 2 m wide, and 2 m deep), and five fault-parallel trenches on the alluvial fan (Tr2, Tr3, Tr5, Tr6, and Tr7, which are 5–8 m long, 2 m wide, and 1–2 m deep). These trenches confirmed that the excavation site is located in a 6 m wide right-stepping relay forming a small pull-apart basin (Fig. 3d,e). In addition, we also excavated several small trenches to expose buried stream channels to constrain the local slip rate. However, these trenches will not be discussed in detail in this study, which focuses on the earthquake chronology of the HFF, except to help to locate the different faults. We identified the main faults bounding the basin from the eastern and western walls of Tr1 and Tr6, as well as from exposures on the lateral walls of the small trenches. In addition, we also observed the secondary faults between the two main branches in the small trenches, accommodating the deformation in the basin (Fig. 3d,e).

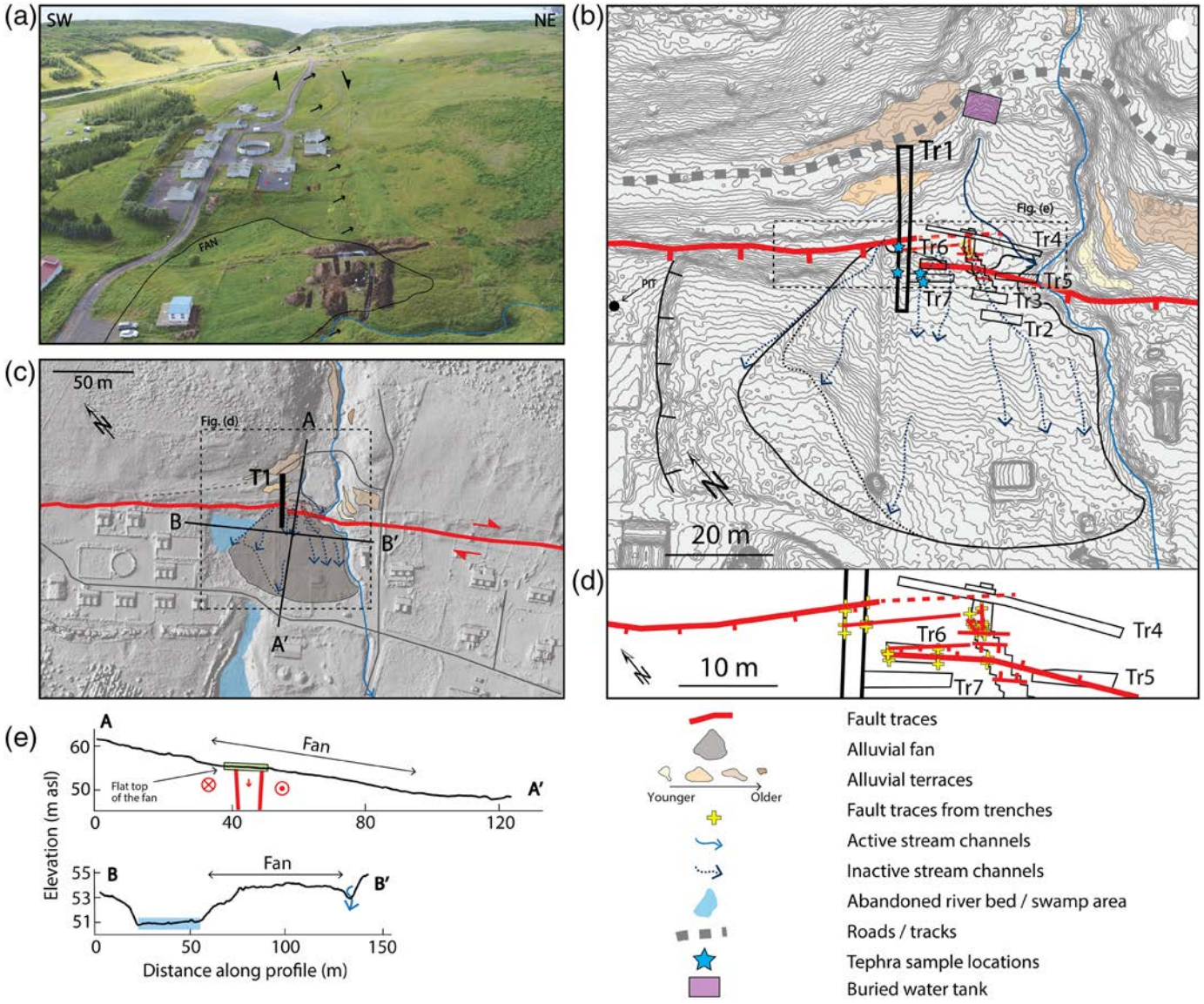


**Figure 3.** The Traðargerði trench site. (a) Northwest looking view of the fault scarp along Laugardalur fault section from the trench site of Traðargerði. The black arrows point at the fault scarp. The excavation site is visible at the bottom of the photograph. (b) Enlargement of the excavation site showing the morphology of the alluvial fan and the fault traces. (c) Morphological map of Traðargerði, north of Húsavík, based on drone-derived digital surface model. The black rectangle represents the location of trench Tr1. (d) Geometry of the fault at the apex of the fan forming a small pull apart basin. (e) Fault-orthogonal (AA′) and fault-parallel (BB′) topographic profiles at Traðargerði with vertical exaggeration of 1.6 and 6.2, respectively. The color version of this figure is available only in the electronic edition.

In the following sections, we will first describe the stratigraphic units found in the main trench of Traðargerði (Tr1), and then we will describe evidence for paleoearthquake ruptures in those trenches.

## Traðargerði stratigraphy

The stratigraphy of Tr1 consists of alluvial deposits, volcanic ash deposits, and soil deposits (Fig. 4). The stratigraphy exposed on the western wall of Tr1 has four main units; a coarse gravel layer defining the base of the trench (Gr), a light brownish clayey layer (layers A and B), dark organic-rich layers containing pieces of birch wood of various sizes (OR and D1–D6), and a chaotic amalgam of clayey and sandy alluvial layers' mix with dark organic layers (marked LS in Fig. 4). In addition, we identified several volcanic ash deposits in the stratigraphy, either in the form of well-defined layers (H3 and H4 in Fig. 4) or sparse lenses (white layers and blue stars in Fig. 4).

One peculiarity of the Icelandic stratigraphy is the presence of ash layers in the subsurface produced by the frequent volcanic eruptions of the volcanoes on the island. Many of these tephra layers are in fact well-documented regionally and can be used as temporal benchmark once they are well recognized (Thordarson and Larsen, 2007; Larsen and Eiriksson, 2008; Thordarson and Höskuldsson, 2008; Gudmundsdóttir *et al.*, 2011, 2012; Lowe *et al.*, 2017; Meara *et al.*, 2020). For example, the layers H3

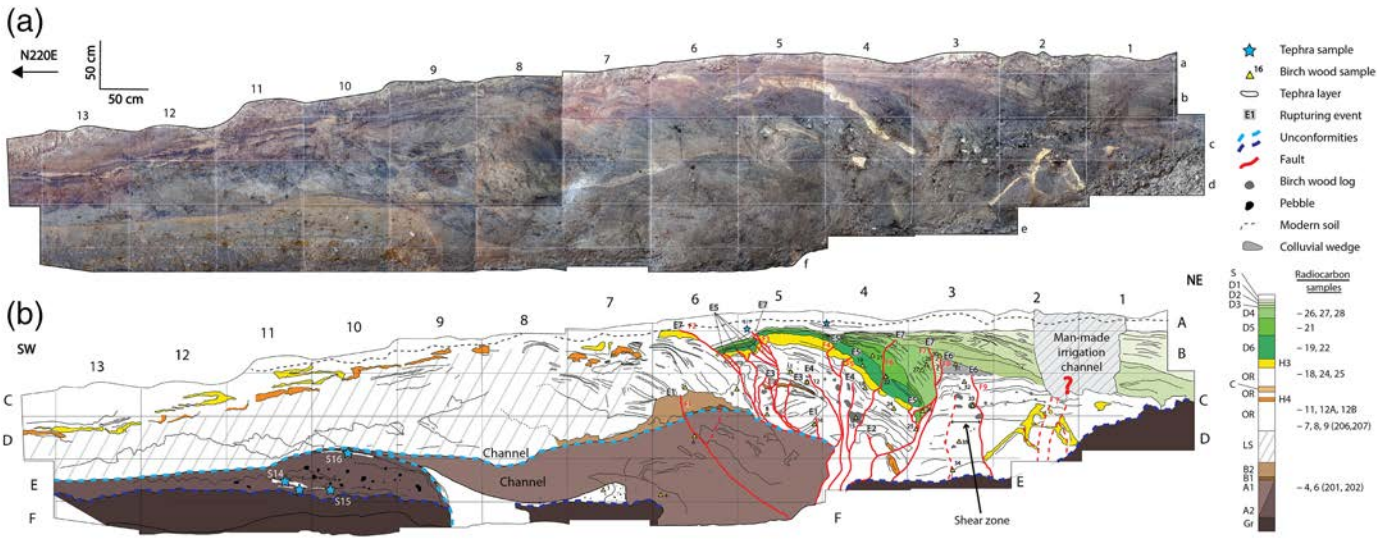


**Figure 4.** (a) Photomosaic and (b) mapping of stratigraphic units and faults of the western wall of Tr1 in Traðargerði. Bottom right shows the stratigraphic log of the western wall of Tr1 with the location of the radiocarbon samples in each layer (numbers on the right). Description of the units: A1 and A2, light brown clayey layers containing some pebbles and two tephra layers (in white and blue stars); D1–D6, grassy organic-rich layers containing small birch logs. Color changes from black to brownish to light yellow; Gr, coarse gravel layer (most likely glacial deposits); H3, Tephra layer Hekla 3; H4, Tephra layer Hekla 4; and LS, clayey sandy speckled "leopard-skin" layer. The color of the patches changes from light brown to black. Most likely alluvial deposits; OR, dark organic-rich layer containing small birch logs. Colors are black and brownish; S, soil. The color version of this figure is available only in the electronic edition.

and H4 are tephra layers with well-known specific characteristics that allow them to be unambiguously identified as Hekla 3 and Hekla 4, respectively, produced by explosive eruptions of the Hekla volcano in south Iceland. H3 and H4 are well documented all over Iceland and present clear characteristics and lithology (Dugmore *et al.*, 1995; Larsen *et al.*, 2002). We identified and sampled six other tephras, four in the unit A2, and two in the topsoil near mark 5.

The gravel unit Gr, at the bottom of Tr1, is visible along most of the trench exposure and is 2 m deep at the deepest point (around mark 7), limiting the depth extent of the trench. Gr is probably a glacial deposit. The top of Gr corresponds to an erosional unconformity (dashed dark blue line in Fig. 4), suggesting that this surface is the base of the postglacial sequence.

The unit A2 is a massive light-brown clayey layer containing pebbles, probably of postglacial fluvial origin. A2 is not continuous laterally, it is visible to the south (mark 9–13) then truncated to the north by a 2.5 m wide channel (around mark 8). A2 is not visible north of mark 8. The top of A2 is an erosional unconformity (dashed light blue line in Fig. 4). We identified four tephra layers in A2: three are embedded in A2 and one is on top of the unit at the erosional unconformity (white patches and blue stars at marks 10 and 11 in Fig. 4, samples S4, S14, S15, and S16).

The unit A1 is a massive clayey alluvial layer extending from mark 5 to mark 9, interrupted by the fault to the north (mark 5). Few sparse disturbed layers are embedded in A1. The 2.5 m wide channel around mark 8 is capped by A1. A1 is up to 1.2 m thick, and the top of the unit is truncated by the same erosional unconformity as the one affecting A2.

The dark units OR and D1–D6 are rich in organic material and confined to the northern part of the trench (mark 1–6) in the vicinity of the fault zone. These units have a grassy texture and contain numerous birch tree logs characteristic of the dry and warm Upper Birch Period (2.5–5 ka B.P., Geirsdóttir *et al.*, 2009; Hellqvist *et al.*, 2020). Units D1–D6 show clear stratigraphy with alternating light and dark layers that are tilt and thicken to the northeast. OR is more massive, even though we could still observe faint layering. OR contains more birch tree logs than units D1–D6.

We located and sampled two tephras embedded in the topsoil about 10–15 cm below the surface at marks 4 and 5. The tephra layer H3 separates the units D1–D6 from the unit OR. The tephra layer H4 is also observed 50–70 cm below H3 embedded in OR. The unit LS is confined to the southern part of the trench (from marks 6–13) above the layer A2. LS consists of chaotic alluvial deposits and patches of organic-rich units and clayey units, with little to no clear layering.

LS is interpreted as remobilized alluvial material from the fan and the upstream gully or patchy soil and peat cover on the alluvial fan. No tectonic deformation could be found in this part of the trench. At this location, the tephra layers H3 and H4 are patchy, close to the surface (5–20 cm deep) and vertically close to each other.

## Evidence for earthquake ruptures in Traðargerði

Most of the following descriptions are based on observations from the western wall of Tr1. The eastern wall of Tr1 remained

wet, and a large part of the wall is disturbed by an old manmade ditch, now backfilled, making its interpretation difficult. However, some of the observations from the western wall are complemented by observations from the eastern wall. The photomosaic and the interpretation of the eastern wall of Tr1 are available in the supplemental material available to this article. The deformation in the trench Tr1 is localized over 4 m between marks 2 and 6 (Fig. 4). No tectonic deformation is visible to the south of mark 6. The central part of the fault zone around mark 5 is characterized by vertical deformation, most likely related to secondary deformation associated with the dip of the fault and the fact that the trench is dug across a small pull-apart basin. This structure is bounded to the south by a small basin between marks 5 and 6 for which we observe rotation and subsidence. To the north at mark 3 a 50 cm wide shearing zone with no preserved layering is bounding the main zone of deformation. This shear zone is sealed by a colluvial wedge, which is itself capped by layer D3. Few additional faults are found below mark 2, whose upper terminations are concealed by an old manmade irrigation ditch (Fig. 4). However, layering in the lower part of the trench indicates that those cracks did not accommodate significant deformation. The upper part of the stratigraphy between marks 5 and 1 is characterized by a set of units D1–D6, which are tilted and thicken toward the north. These units are interrupted between marks 1 and 2, down to 1 m, by the old abandoned irrigation ditch. In addition, just north of mark 1, two water pipes are crossing the top of the trench, whereas the gravel base is becoming shallower, marking the northern end of the alluvial fan deposits. Hence, we assume that no major fault exists north of the pipes, because no significant deformation is observed in the upper part of the trench.

Following the approach from Scharer *et al.* (2007), we define three categories of likelihood (likely, probable, and possible) for a single evidence or a set of evidence to correspond to earthquake-induced deformation. We based our ranking on three criteria: the type of evidence, the quality of the evidence, and the number of evidence per event. The most common evidence that we observed at Traðargerði and Vestari-Krubbsskál are upward terminations of faults and cracks that vertically offset sedimentary units. In addition, we used the folding of units observed only in Traðargerði as evidence. In some cases, we used liquefaction features or opening and subsequent filling of fissure as evidence for earthquakes, although this kind of evidence is found only in Vestari-Krubbsskál. The quality of an evidence is defined by its strength of expression (Scharer *et al.*, 2007; Rockwell *et al.*, 2015). For example, an observation that can only be explained by earthquake-induced ground deformation (e.g., clear offset of sedimentary units or seismic liquefaction features) will have a high score, whereas an observation that could be explained by other processes (e.g., ice wedge or thufur in periglacial environment like Iceland) will have a lower score. Finally, the number of evidence may also

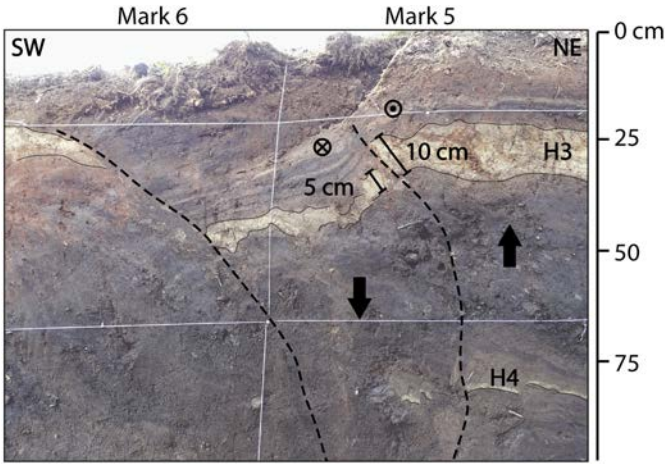


**Figure 5.** Photograph of the small basin at the top of the western exposure of Tr1 between mark 5 and 6 showing significant change of thickness in the tephra layer Hekla 3 (H3). This sharp difference of thickness in the layer is interpreted as horizontal displacement. The black arrows show vertical motion; the cross and the dot show the horizontal motion. The color version of this figure is available only in the electronic edition. 24

affect the ranking, particularly for ambiguous observations (Scharer *et al.*, 2007). Indeed, evidence of events of moderate-to-low quality will become significant if they are numerous. In contrast, single high-quality evidence would be sufficient to be classified as likely, because it has no other interpretation than being the result of an earthquake-induced deformation.

We identified seven events in Tr1, labeled E1–E7, E1 being the deepest event observed in this trench. Four events (E3, E5, E6, and E7) are associated with clear coseismic deformation rupturing the surface. Three other events (E1, E2, and E4) are more ambiguous, because their deformation is less evident. It is important that we observe vertical deformation in an oblique strike-slip context; therefore, reporting mainly secondary deformation from earthquake ruptures. In some cases, we can observe lateral change of thickness of the same sedimentary units across a fault zone that is interpreted as a horizontal displacement (Fig. 5). Indication of earthquake ruptures for the seven events we recognized are described subsequently. The amplitudes of the vertical coseismic displacements associated with each event are summarized in Table 1.

E1 is the deepest event in Tr1. It is associated with two faults. F1 cuts through the layers A2 and B1, and stops just above B2. E1 is associated with 1–4 cm of vertical displacement along F1. However, the amount of displacement seems larger at the contact between A2 and B2 than at the top of B2, suggesting that more than one event may have occurred along F1 (Fig. 4). The second fault associated with E1 bounds the northern edge of A2 between marks 4 and 5 and stops ~20 cm above the erosional unconformity, right below a triangular rotated block. However, this fault does not show any vertical displacement (Fig. 4). E1 shows the evidence of earthquake-

TABLE 1
**Summary of the Vertical Coseismic Displacements Observed in Tr1 in Traðargerði and VK1 in Vestari Krubbsskál**

| | Vertical Deformation | | Ranking | |
|---|---|---|---|---|
| **Event** | **Tr1 (cm)** | **VK1 (cm)** | **Tr1** | **VK1** |
| E9 | – | 2–3 | – | Probable |
| E8 | – | 2–3 | – | Possible |
| E7 | 5–10 | – | Likely | – |
| E6 | ~15 | – | Likely | – |
| E5 | 4–7 | 12 | Likely | Likely |
| E4 | Deformed | – | Possible | – |
| E3 | 2–3 | 7–8 | Likely | Likely |
| E2 | Deformed | 3–4 | Possible | Probable |
| E1 | 1–4 | 5–6 | Probable | Likely |
| Event a | – | 5–7 | – | – |

related deformation along F1, but E1 is associated with only two faults. Therefore, we classify E1 as probable.

E2 is associated with only one crack stopping just below a folded layer at mark 4 (Fig. 4). This layer does not have the characteristic lithology of the tephra layer H4 but seems to correspond laterally to H4. The crack does not show displacement, but it seems to have deformed the top layer and filled a small fissure. The evidence for E2 is few and ambiguous. Therefore, we categorized E2 as possible.

E3 is confined to the central part of the fault zone localized within 25 cm around mark 5 (Fig. 4). E3 is associated with three cracks with a clear vertical offset of H4 of 2–3 cm along each crack (Fig. 6), but no significant change in thickness (i.e., horizontal motion) is visible. The event horizon is a thin black layer located a few centimeters above H4. The coseismic displacement along the three cracks is clear; therefore, we categorized E3 as likely.

E4 consists of two cracks located between marks 4 and 5 (Fig. 4). The two cracks stop within the massive thick dark grassy layer OR (Fig. 6b). Therefore, we do not identify a well-defined event horizon for E4. In addition, the cracks do not have vertical displacement. Hence, E4 is categorized as possible.

E5 is associated with at least seven cracks showing clear vertical displacement (Fig. 4). The deformation is localized in the small basin between F2 and F3 at marks 5 and 6 (Fig. 6a) and along F4 and F5 at mark 4 (Fig. 6b). We observe a clear change of thickness of H3 on each side of F3, in which H3 is 5–7 cm thick southwest of F3 and 12–15 cm thick northeast of F3, suggesting significant horizontal deformation. Further north, around mark 4, E5 breaks H3 along F4 and F5 in which H3 is displaced downward. The vertical displacement along F4 is 4–7 cm. From marks 4 to 5, H3 is rotated clockwise whereas around mark 2, H3 is rotated anticlockwise, suggesting motion along the shear zone during E5. E5 breaks H3 and stops in layer D6 (Fig. 6). H3 at mark 2 is highly broken and deformed. The evidence of coseismic displacement associated with E5 is clear; therefore, we categorized E5 as likely.

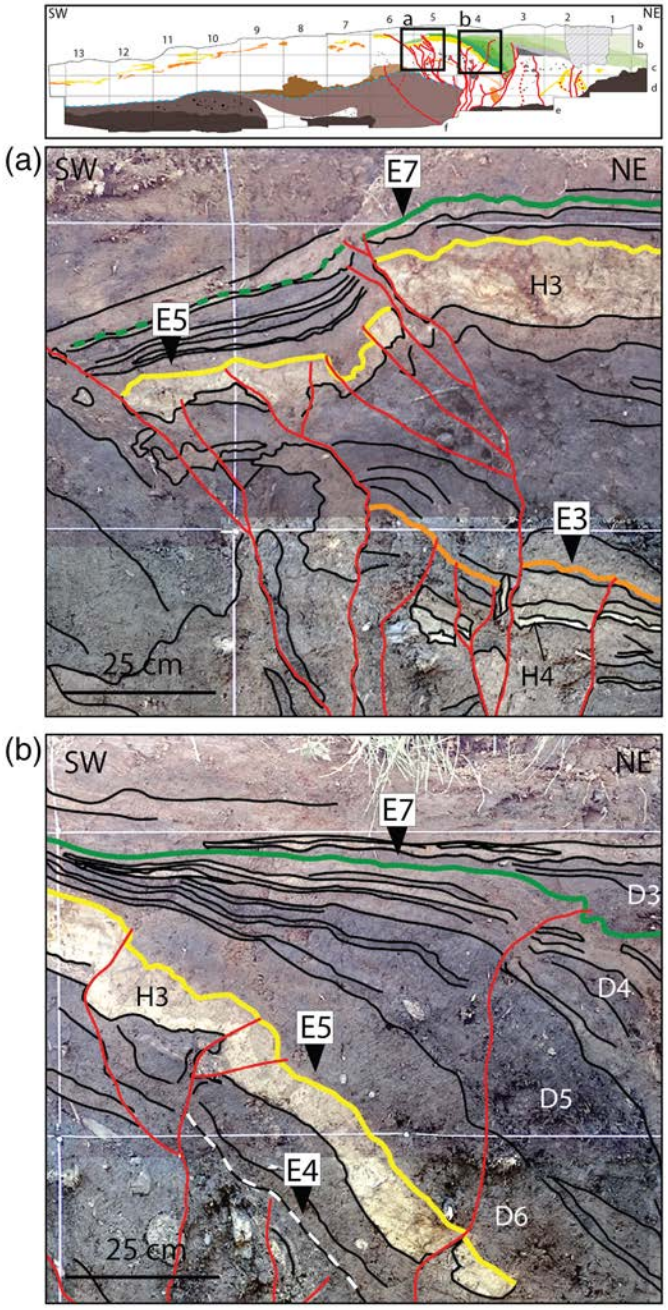


**Figure 6.** Photographs showing examples of earthquake horizons in Tr1 in Traðargerði. Panels (a) and (b) show enlargements of the trench wall of Tr1 where earthquake ruptures and earthquake horizons are clearly visible. The orange, yellow, green, and dashed white lines represent the earthquake horizons of E3, E5, E7, and E4, respectively. The color version of this figure is available only in the electronic edition. 25

E6 probably activated F8 and F9, already activated by E5. The tops of layers D5 and D6 are tilted northward between marks 3 and 4, which means D5 and D6 are probably deformed by E6 (Fig. 4). Similarly, the stratigraphy inside D4 suggests that D4 was deformed by E6, although the near-horizontal top of D4 would suggests filling up of accommodation space. The deformation of D4–D6 is due to the activation of the shear zone

between F8 and F9 during E6 (Fig. 4). Finally, we observed ~15 cm of vertical displacement along F8. E6 was then sealed by a colluvial wedge at mark 3, most likely formed by material coming from the layer D4. Although E6 is associated with only two faults, the colluvial wedge is strong evidence of earthquake-induced deformation. Therefore, we categorized E6 as likely.

The most recent event in Tr1 is E7. It is clearly visible in the western wall of Tr1, located about 20 cm below the present-day surface and associated with F2, F3, F6, and F7 (see horizon E7 in Figs. 4, 6). Between F2 and F3 at marks 5 and 6, E7 has rotated the stratigraphy inside the small basin from the layer H3 upward (Fig. 6a). The dip slip on F2 and F3 reaches 5–10 cm, although we cannot exclude that part of this slip is due to the event E5. Along F6 and F7 at marks 3 and 4, E7 breaks the top of the layer D4 and is sealed by the layer D3 (Fig. 6b). In addition, a crack opened between F7 and F8 during E7 that was then eventually filled with material from D3 when D3 capped E7. The vertical deformation along F6 and F7 is only a few centimeters. E7 activated four faults and is associated with significant vertical deformation. Therefore, we categorized E7 as likely.

## VESTARI-KRUBBSSKÁL

### Vestari-Krubbsskál morphology

Vestari-Krubbsskál is a pull-apart basin located ~1.5 km southeast of Botnsvatn lake at 320 m (Fig. 2) within the gentle slopes of the interglacial shield volcano Grjótháls (Sæmundsson *et al.*, 2012). Similarly to Traðargerði, we collected 1892 aerial photographs using an UAV and we computed the orthomosaic map and the DSM using eight ground control points to correct the map reconstructions, achieving a resolution of 2.84 cm/px and 4.89 cm/px, respectively (Fig. 7).

Vestari-Krubbsskál is a closed basin where drainages converge, allowing for optimal sediment deposition and preservation. The basin is of triangular shape, narrowing toward its southeastern termination. It is 500 m long at the longest, 200 m wide, and 50–60 m deep (Fig. 7). The basin is bounded by the main fault trace along its southwestern edge and by two secondary faults along the northeastern side. Although no obvious trace of the recent activity of the fault could be found in the morphology of the basin, the northernmost secondary fault, which cuts through exposed bedrock, shows a clear cumulative right lateral offset of 20 ± 2 m consistent for the three nearby stream channels (Fig. 7). A few tens of meters westward along the same fault, a single, cumulative displacement of 90 ± 10 m offsets a larger stream channel. A small right step in the main fault trace seems to accommodate a smaller secondary basin at the western corner of the main basin (where trenches VK1 and VK2 are located).

We excavated four trenches in Vestari-Krubbsskál: two across the main fault trace (VK1 and VK2, which are 26 m long, 2 m wide, and 3 m deep and 50 m long, 1 m wide, and 2 m deep, respectively) and two across a secondary fault bounding the northern edge of the basin (VK3 and VK4, which are 20 m long,

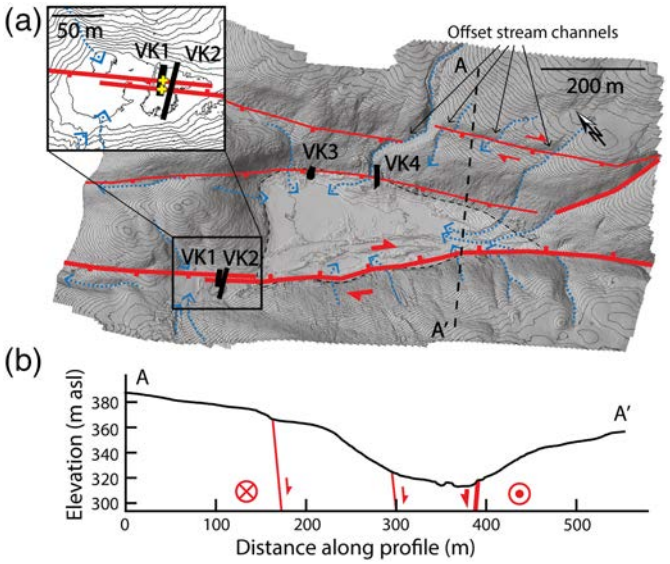


**Figure 7.** (a) Map of the Vestari-Krubbsskál site east of Húsavík based on drone-derived digital surface model (DSM). The thick and thin red lines show the main and secondary fault strands, respectively. The thick black lines mark the four trenches excavated in the basin (VK1–VK4). The top left box is an enlargement of the VK1 and VK2 trench locations. The black dashed line represents the topographic profile shown in panel (b). The vertical exaggeration in panel (b) is 1.4. The color version of this figure is available only in the electronic edition.

6 m wide, and 3 m deep and 36 m long, 2 m wide, and 2 m deep, respectively). Trenches VK3 and VK4 show a few centimeters of vertical displacement and no evidence, even indirect of horizontal motion, suggesting that the northern fault accommodates only secondary deformation. The northernmost fault strand where the right lateral offsets are visible is located upslope in bedrock, therefore no trenches could be excavated. In trenches VK1 and VK2, it is possible to see evidence for large deformation, suggesting that the southern strand is the most active fault trace.

### Vestari-Krubbsskál stratigraphy

In contrast with Traðargerði, Vestari-Krubbsskál is a pull-apart basin, and therefore its stratigraphy consists mainly of flat, well-defined layers (Fig. 8). In the following, we describe the stratigraphy and earthquake evidence based on the exposure of the eastern wall of VK1 (Fig. 8). Consistent observations are also seen on other walls (see supplementary material), although bad weather conditions prevented us from mapping them in detail. We can distinguish four main sedimentary packages: a set of gray to orange bedded fine sand and clay layers at the bottom of the northern section of the trench (marks 14–19, unit A in Fig. 8), a 50 cm thick beige sand and silt layer (B1), a 1.5 m thick brown to orange sand layer in the central section of the trench (marks 7–16, units B2–B4 in Fig. 8), and a 50 cm thick light-brown soil containing fine sand and four tephra layers.

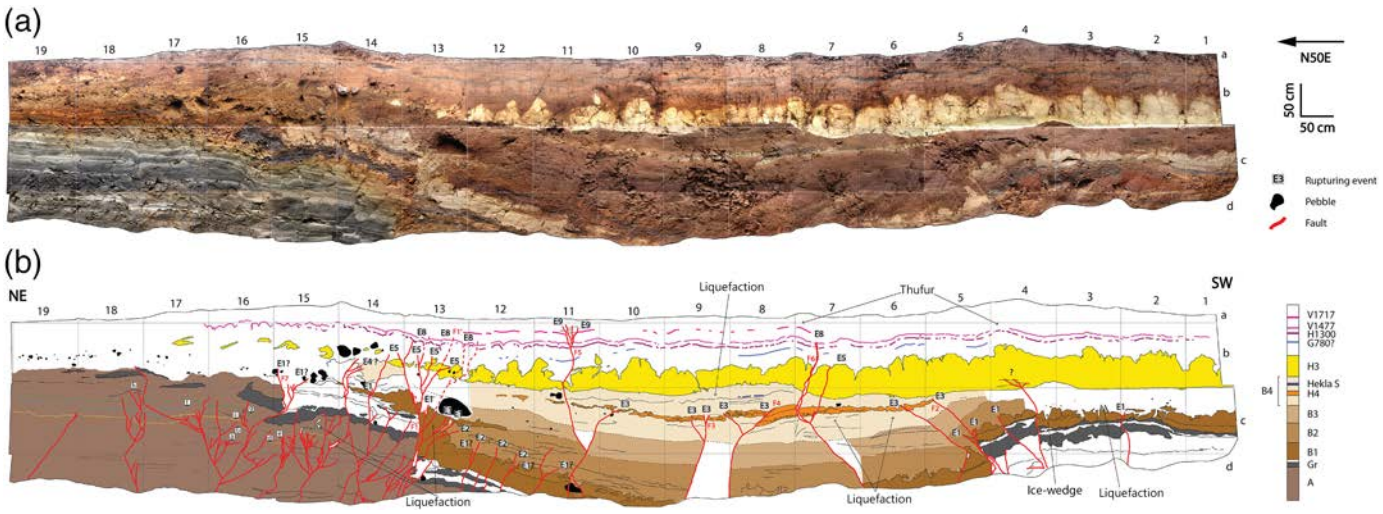


**Figure 8.** (a) Photomosaic and (b) mapping of stratigraphic units and faults of the eastern wall of VK1 in Vestari-Krubbsskál. Bottom right shows the stratigraphic log of the eastern wall of VK1. Description of the units: A, bedded sand and clay layers; B1, massive sand and silt layer; B2, B3, and B4; massive pebbly sand layers; Gr, gravel layer; H4, Hekla S; and H3, G780, H1300, V1477, and V1717, tephra layers. The color version of this figure is available only in the electronic edition.

Unit A is likely of lacustrine origin, probably from late glacial to early postglacial period, when climate was warmer and coastal areas were ice free (i.e., Allerød age to Younger Dryas, around 13–12 ka B.P., Geirsdóttir *et al.*, 2009; Ingólfsson *et al.*, 2010). Unit A is capped by a 10–20 cm thick layer composed of coarse sand with gravels, probably corresponding to glacial outwash deposits from the end of the readvance of the glaciers during the colder Younger Dryas (around 11 ka B.P., Ingólfsson *et al.*, 2010).

Unit B1 is a compact sand and silt layer, probably corresponding to swamp deposits from a wetter period such as the Earlier Swamp Period (7–5 ka, also called the Lower Mire Period, Hellqvist *et al.*, 2020). The Earlier Swamp Period is characterized by a more humid climate resulting in the development of wetlands in Iceland.

Units B2–B4 are mostly massive aeolian deposits of medium-to-fine sand and fining upward. Some faint stratigraphy can be observed, especially in B2, but this stratigraphy is not well defined. B2–B4 contain some pebbles and boulders, mostly on the northeast side of the trench, probably due to the proximity of the southwest facing slopes just north of VK1 (Fig. 8).

In addition to the sedimentary layers, we identified the same two characteristic tephra layers Hekla 3 and Hekla 4, as in Traðargerði. H3 and H4 in Vestari-Krubbsskál are significantly thicker than in Traðargerði (up to 70 cm and 15 cm, respectively) due to the better accumulation and preservation settings of a pull-apart basin. The tephra layer Hekla 4 is visible only in the central part of the trench in the form of small lenses. The tephra layer Hekla 3 is up to 50 cm thick to the southwest of the trench exposure, thinning toward northeast and preserved only as small localized patches at the northeast end of the trench. The top of H3 is highly disturbed by frost processes, mainly cryoturbation and ice wedging (see supplemental material). In contrast to the top of H3, the base of H3 is very smooth and seems to seal the previous topography. Although the trenches VK3 and VK4 turned out to be of limited interest to define earthquake events, they were of some use to define the temporal framework.

In addition, we identified four tephra layers in the soil section above H3. The lowest one called G780 is not laterally continuous in VK1 but shows as few lenses in the central part of the trench from marks 5 to 12. The next two tephra layers are laterally continuous in the trench and vertically close to each other, 5–7 cm apart. The lower one is called H1300, and the shallower one is called V1477. Similarly to G780, the highest tephra layer that we identified is patchy, mainly located in the central part of the trench. This layer is called V1717 and is located 20–30 cm below the surface. For instance, we identified in VK3 a well-documented, early Holocene tephra layer Askja S embedded in the lacustrine unit A (see supplemental material).

In addition to tectonic deformation, due to the nature of the sediments at the site of Vestari-Krubbsskál, mostly sand to clay, numerous soft-sediment deformation structures (SSDS) could be observed in our trenches. However, one has to be careful in the interpretation of the SSDS in periglacial environment, because the deformation can be related to periglacial processes as well as seismic processes (Müller *et al.*, 2021). We used the following criteria as evidence for earthquake-induced SSDS: the sudden formation of the SSDS (Wheeler, 2002), the comparison of the observed structures with well-known and well-identified earthquake-induced SSDS (Owen and Moretti, 2008), and the lateral continuity of the affected layer (van Loon *et al.*, 2016).

We identified several earthquake-induced SSDS referred to as liquefaction features in the eastern wall of VK1 (Fig. 10). Well-developed flame structures affect layer B1 and are injected upward in layer B2 at marks 3 and 13 (Fig. 10). These flame structures are laterally continuous in B1. In addition, tephra

layers H3 and H4 are affected by downward injections that are fluid-driven fractures filled with the material of the impacted layer. These filled fractures are observed all along the base of H3 and H4 but mostly from marks 6 to 9. These filled fractures contain nonstratified, uniform material, indicative of sudden formation (Wheeler, 2002). Finally, we observed a 4 cm wide clastic dike at mark 15, injected downward in the lacustrine layer A, around 10 cm below the gravel layer. Clastic dikes are most commonly formed during earthquake by rapid injection of fluid due to over pressure. Aside from SSDS related to earthquakes, several SSDS due to periglacial processes can also be observed in Vestari-Krubbsskál (Fig. 8), which include cryoturbation, ice wedging, or thufur (see supplemental material). Cryoturbation is the mixing of soil material due to repeated freezing and thawing of the surface and subsurface ice. Ice wedging is the process in which a crack is filled with water that freezes and consequently expands and enlarges the crack. Thufur, also called frost bumps, are small mounds formed by the seasonal freezing and thawing of the ground. These nontectonic processes are usually limited to the top of the trench.

## Evidence of earthquake ruptures at Vestari-Krubbsskál

The main structure of the trench VK1 is a 9 m wide pull-apart basin bounded by two main fault zones (Fig. 8). The northeastern bounding fault F1 at mark 13 is nearly vertical and separates the early postglacial lacustrine unit A to the northeast from the subaerial sedimentary units B (2–4) to the southwest. The vertical displacement is mainly accommodated by the two bounding faults F1 and F2 (marks 13 and 5, respectively), and the maximum-localized vertical displacement is observed along F1. The cumulative vertical displacement is about 60–65 cm along F1, in which the layers A and B1 are visible on both sides of the fault and clearly vertically offset (Figs. 8, 11c). The southwestern-bounding fault F2 reveals a pop-up structure (around marks 4 and 5 in Fig. 8 and Fig. S6b), probably resulting from local compression along-strike due to the dominant strike-slip motion. F2 seems to not propagate up to the surface but instead to stop below the tephra layer Hekla 3 (see around marks 4 and 5 in Fig. 8). The two bounding faults F1 and F2 are clearly reactivated by multiple seismic events. No significant subsidence of the central part seems to have occurred since the emplacement of the layer Hekla 3. In addition, the flame structures in B1 observed at marks 3 and 13 are likely liquefaction features associated with an earthquake occurring sometime after the deposition of B1 (Fig. 10c,d).

We identified three events (E1, E3, and E5) with significant coseismic deformation and three more ambiguous events (E2, E8, and E9) for which coseismic deformation is less evident. Some sedimentary units are massive (B2–B4 for instance), making it difficult to identify fault terminations or earthquake horizons. We used the tephra layers identified in Traðargerði and Vestari-Krubbsskál as anchors to correlate the trenches from the two locations. Then, we used Tr1 in Traðargerði, where we dated layers as a reference trench to identify and date the events in VK1 in Vestari-Krubbsskál. The correlation of the trenches is discussed in more detail in the Results section. Therefore, the labeling of rupturing events and earthquake horizons (e.g., E1) is consistent between Traðargerði and Vestari-Krubbsskál (e.g., E1 in Traðargerði is the same event as E1 in Vestari-Krubbsskál). Because there are only one or two events between known tephras, and based on the stratigraphic position of the events and due to the proximity of the two sites, we assume that the events observed in Traðargerði are the same than the events observed in Vestari-Krubbsskál. The earthquake ruptures associated with the six events are described subsequently. The amplitude of the vertical coseismic displacements associated with each event is summarized in Table 1.

The event E1 is visible on the two bounding faults F1 and F2 (Fig. 8) and associated with 8–10 cracks, including isolated cracks at marks 11 and 12 (Fig. 9b). E1 is also identified by the thickening of unit B2 that most likely filled the basin after E1 (Fig. 9c). E1 broke all the way to the top of layer B1, defining the earthquake horizon. Therefore, we categorize E1 as likely.

The event horizon associated with the event E2 is not well constrained, because it appears to stop within the massive unite B2 (Fig. 8). E2 consists of four individual cracks reaching the sedimentary unit B2 in the subsiding section of the trench at mark 12 (Fig. 9). The upward terminations of E2 seem to be located within the unit B2, 20 cm above B1. The vertical coseismic displacement associated with E2 is 3–4 cm. No clear earthquake horizon can be defined for E2, but we observed clear coseismic deformation along four cracks. Therefore, we categorized E2 as probable.

E3 is associated with several cracks along the faults F2–F4, localized in the central part of the trench (marks 5–10), in the subsiding part (Fig. 8). The event horizon is the top of the tephra layer Hekla 4. Along F4, at mark 8, the layer H4 is offset vertically, and the thickness H4 changes drastically from 10 cm to the north of the fault to 20 cm to the south of the fault (Figs. 9c, 11b). The change of thickness probably results from significant lateral motion on the fault. Along F2, at mark 5, the layer Hekla 4 stops abruptly, either truncated by the fault or eroded away from the top of the pop-up structure (Fig. 9d). In addition, downward injection-filled fractures are liquefactions features likely associated with E3 (Figs. 9c, 10g). The evidence for E3 is clear. Hence, E3 is categorized as likely.

The event E4 is associated with a single fault at mark 14, showing no evidence of motion and likely stopping in unit B4 (Figs. 8, 9). Therefore, we suggest that the occurrence of E4 in VK1 is unlikely and thus does not account for it.

The event E5 is associated with faults F1 and F6 (Fig. 8). The earthquake horizon for E5 is the top of the layer Hekla 3. Along F1, the event E5 is characterized by a set of cracks breaking H3 into small chunks and interrupting H3 (Fig. 9b). The main displacement associated with E5 is a vertical motion of 12 cm

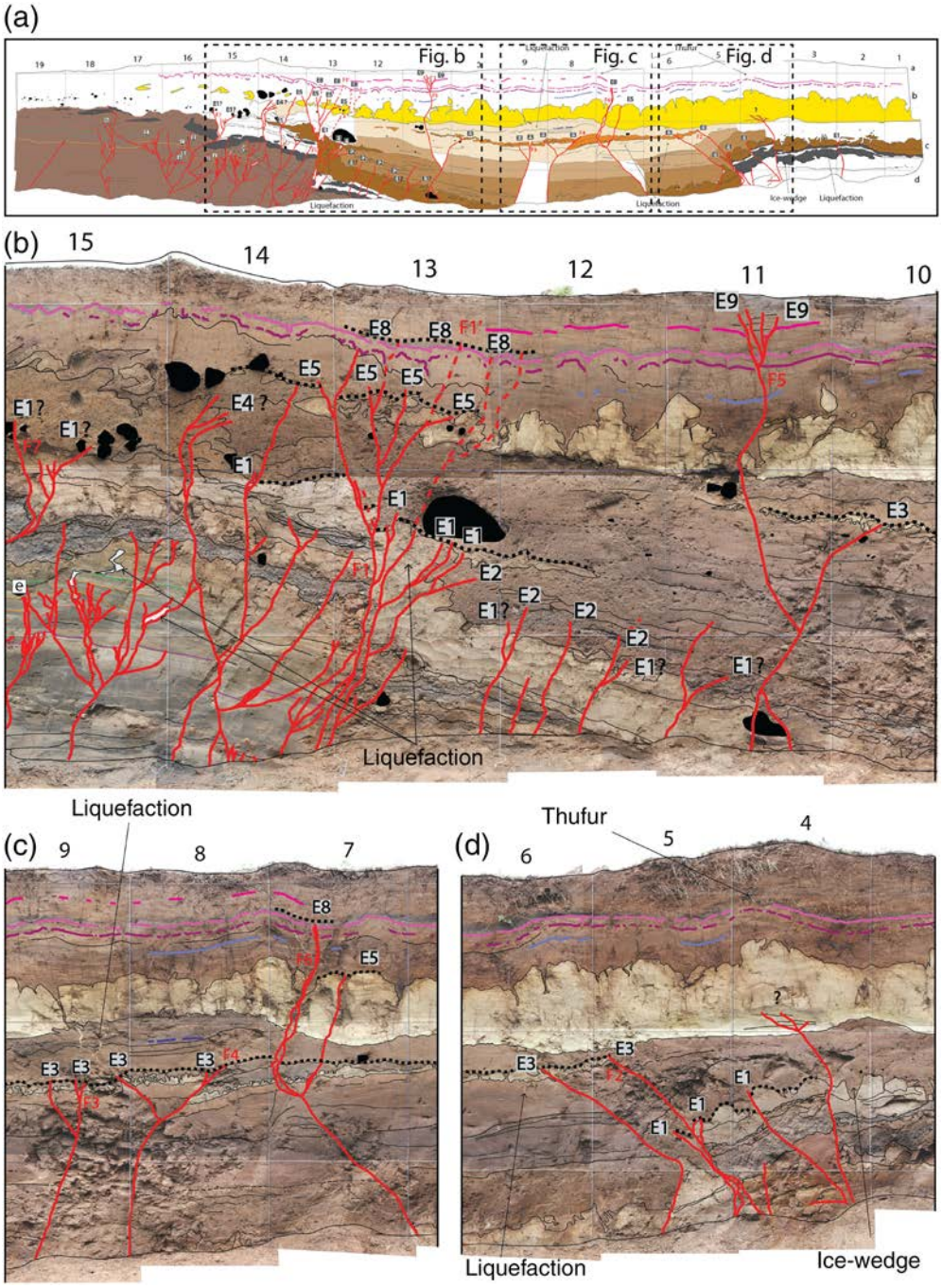


**Figure 9.** Trench logs showing stratigraphy, faults, and earthquake horizons in VK1. (a) Complete interpreted trench log for VK1 and (b–d) Enlargements of the interpreted trench log superimposed on the mosaic photographs of the trench exposure. The locations of panels (b–d) are shown in panel (a). The purple lines represent the tephra layers, as presented in the stratigraphic log in Figure 8. The thin black lines show the stratigraphic units as mapped in Figure 8. The black dotted lines are the earthquake horizons, labeled E1–E9. The color version of this figure is available only in the electronic edition.

along the fault F1′ from the set of faults F1 at mark 13. Along F6, the fault stops on top of the layer Hekla 3. However, no displacement seems to be associated with this crack. It is important that coseismic displacement is not easy to determine for the event E5, because the top of Hekla 3 layer is irregular and deformed due to periglacial deformation processes mentioned earlier (Fig. 9c). However, we observed downward injection-filled fractures at the base of H3 that are liquefaction structures most likely associated with E5 (Fig. 10f). Evidence for E5 is numerous, and the vertical offset is clear. Therefore, we categorized E5 as likely.

Event E8 is associated with the same faults as E5, F1 at mark 13 activating several faults, and F6 at mark 7 activating a narrow shear zone of 1–3 cm wide (Fig. 8). Along F1, a set of cracks breaks through the tephra layer V1477 and seem to stop just above V1477 (Fig. 9b). However, these cracks are not well identified, and the displacement associated with these cracks is small or nonexistent. Along F6, the fault trace is clearer, and it breaks the tephra layer V1477 (Fig. 9c). But similarly to F1, little to no displacement is visible (2–3 cm). Hence, E8 is categorized as possible.

The event E9 is the shallowest and the youngest event that we identified (Fig. 8). E9 is characterized by only one fault termination, F5, at mark 11, forming two V-shaped sets of cracks (Fig. 9b). These V-shaped sets of cracks are not fissures opening and filled but cracks disturbing the existing layering. E9 interrupts the tephra layer V1717. The vertical displacement associated with E9 is 2–3 cm. E9 is based on a single observation, but there is no ambiguity on this observation. Therefore, we categorized E9 as probable.

In addition, we identified five earthquakes in VK1 from fault terminations (marked a–e in Fig. 12) in the lacustrine deposits (unit A). Unfortunately, no age constraints are available for these events, and none of these events were identified

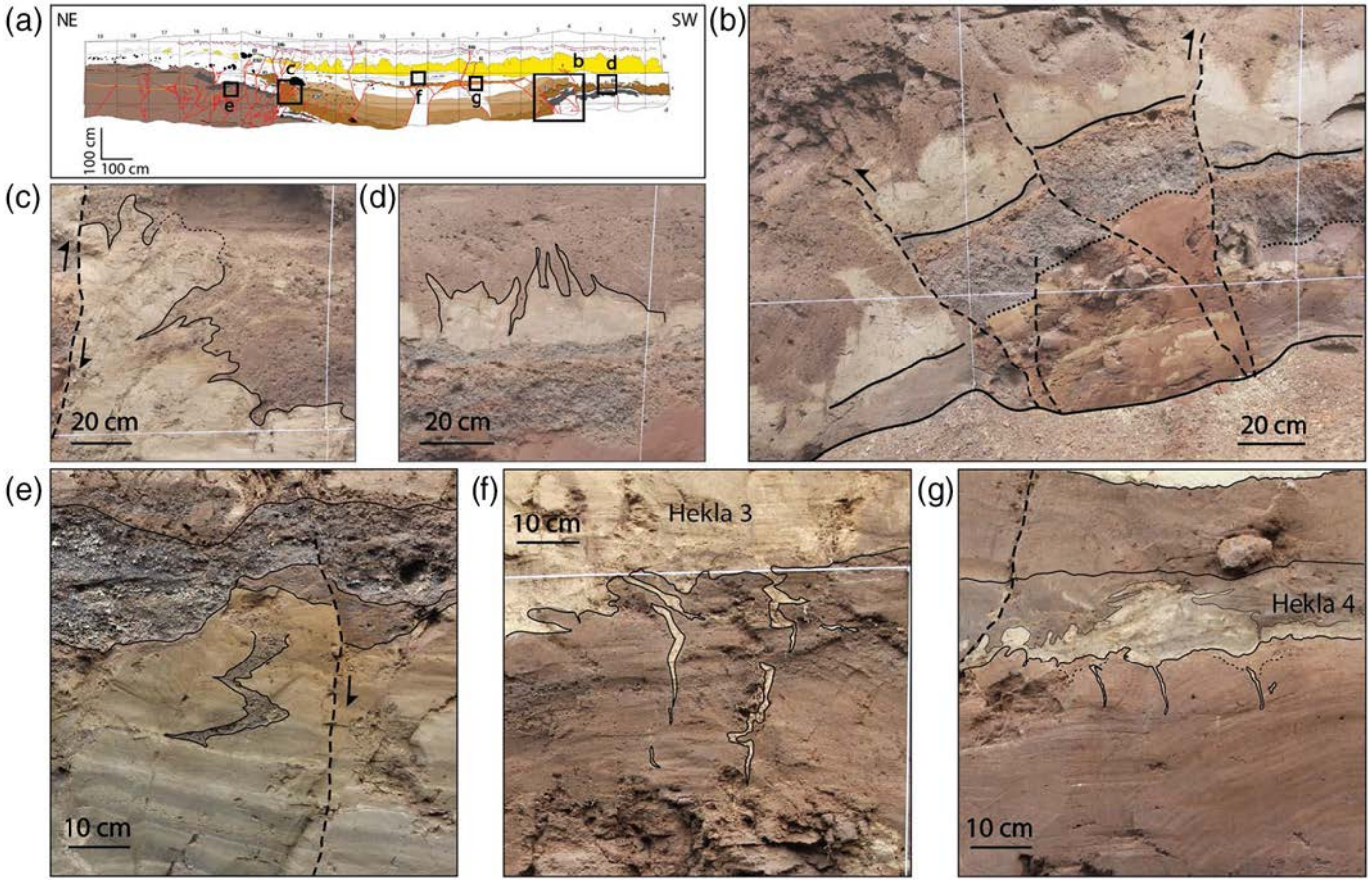


**Figure 10.** Features observed in the trench VK1 in Vestari-Krubbsskál. (a) Simplified section of the eastern wall of VK1 showing the locations of (b–g). (b) Compressional feature on the bounding fault of the basin. Different liquefaction features are visible in VK1 in the form of seismites (or flames) in the layer B1 (c, d), of clastic dike in the gravel layer (e), of sandy dikes in the Hekla 3 (f), and in Hekla 4 (g) tephra layers. The color version of this figure is available only in the electronic edition.

in Tr1. Therefore, we do not include them further in our analysis. However, almost no vertical displacement is associated with these events, and deformation is mostly seen through cracks and disturbed layers. Therefore, either we suppose that most of these events correspond to smaller magnitude events (M <6) and are being recorded because of the "high-resolution" thin-bedded stratigraphy of unit A or some of them could have been larger events whose evidence for main deformation are buried deeper than the bottom of the central part of our trench (marks 5–13) and were not exposed during the excavation. Only "event a," associated with 16 fault and crack terminations (purple layer in Fig. 12), seems to show significant vertical deformation from a single event, up to 5–7 cm, suggesting an earthquake somehow larger than the other ones observed in unit A in VK1. The location of "event a" low in the unit A suggests a timing sometime after the deposition of the tephra Askja S ~10 ka ago during the early Holocene.

## AGE CONSTRAINTS

We use radiocarbon dating to constrain the timing of the events in Traðargerði. No radiocarbon datable material was found in Vestari-Krubbsskál. We used the tephra layers identified at both the sites as anchor to correlate the two trenches Tr1 and VK1. Trench Tr1 contains abundant small birch tree logs. The layers D4–D6 and OR are richer in birch logs than others. These organic-rich units correspond to the well-documented Later Birch Period all over Iceland, a 2500 yr long warm period, favorable to birch growth, lasting from 5000 to 2500 B.P. (Geirsdóttir *et al.*, 2009; Hellqvist *et al.*, 2020). We collected 36 birch samples from the western wall of Tr1 and 20 birch samples from the eastern wall of Tr1. Most samples are small twigs 10 cm long or less to limit the possibility of in-built age (Rizza *et al.*, 2019). Out of these 56 samples, 31 samples were sent for radiocarbon analysis (Table 2), which cover the entire exposure of the trench section in the vicinity of the fault zone. The uncalibrated radiocarbon ages range from 2260 ± 15 B.P. to 7565 ± 15 B.P., with increasing ages consistent with the stratigraphic order. Only two samples— samples 6 and 205 (7545 ± 15 B.P. and 7565 ± 15 B.P., respectively)— are out of stratigraphic order. However, these two samples are located close to a fault, and therefore they have likely been displaced by faulting activity. Four samples (32–35) have similar age (Table 2), although they are spread vertically over 1 m (see mark 3 of the trench Tr1 in Fig. 4). We explain this distribution

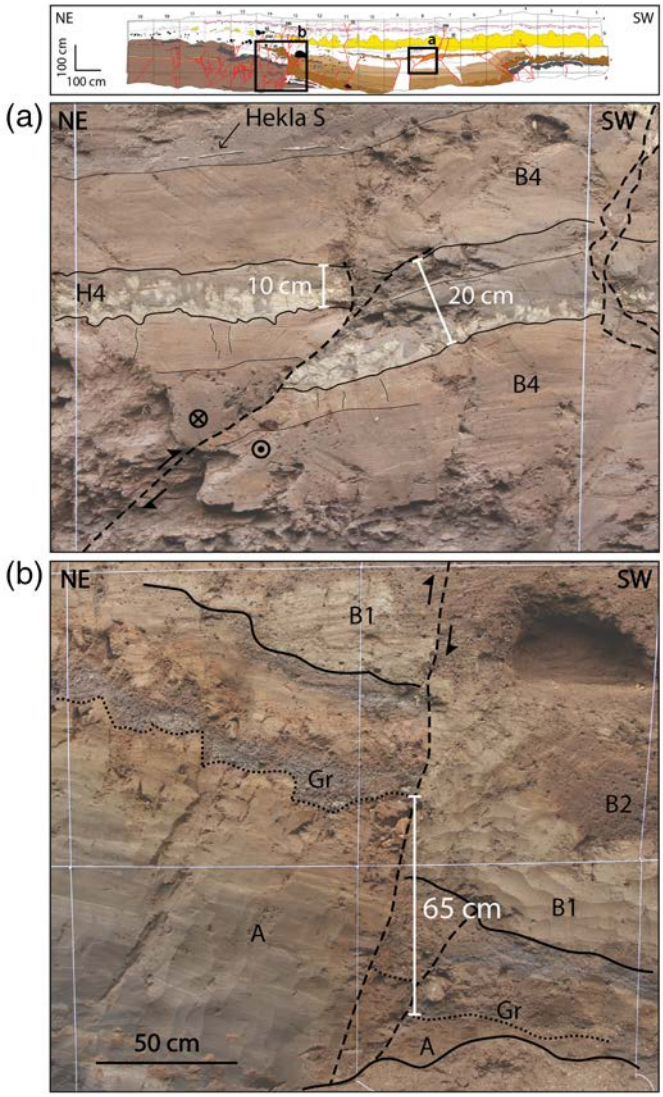


**Figure 11.** Photographs from the eastern wall of VK1 showing examples of (a) coseismic horizontal displacement observed through change of thickness in the tephra layer Hekla 4 and (b) the maximum cumulative vertical displacement observed. The color version of this figure is available only in the electronic edition.

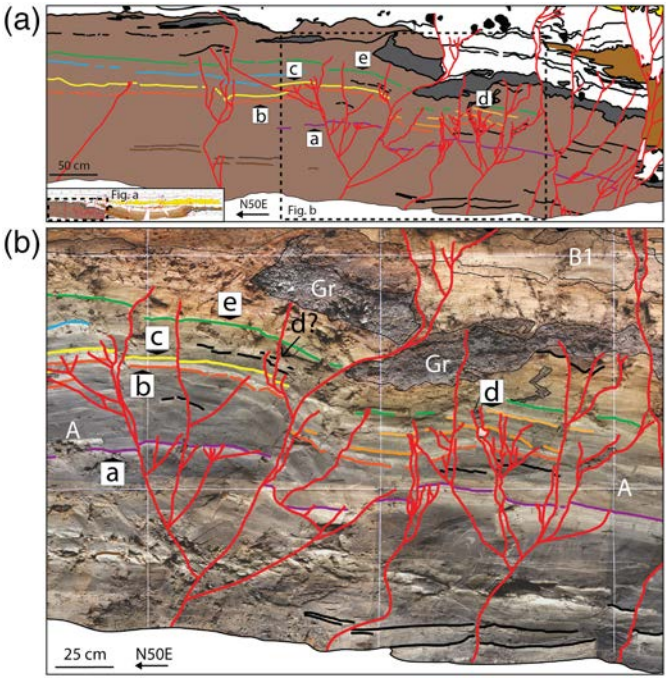


**Figure 12.** Evidence of ruptures in the lacustrine sediments of VK1 in Vestari-Krubbsskál. (a) Northernmost section of VK1. The colored horizontal lines represent earthquake horizons and thin-bedded sand layers in the lacustrine unit A. The earthquake horizons are labeled from (a) to (d). The dashed frame indicates the location of panel (b). (b) An enlargement of the eastern wall of VK1. The event horizon "a" (purple) shows the most coseismic vertical displacement up to 7 cm. The color version of this figure is available only in the electronic edition.

of the samples by the activation of a wide shear zone between the fault F9 and the inferred dashed fault at mark 3 (Fig. 4) during an event.

In addition to radiocarbon analysis, we used the tephras produced by volcanic eruptions to constrain the ages of the seismic events. We sampled 17 layers (labeled S1–S17) from four different vertical soil sections in Traðargerði (blue stars in Fig. 3) and 16 layers from three different soil sections in Vestari-Krubbsskál. To identify the volcanic system associated with each tephra and to discriminate tephras produced by different eruptions of the same volcanic system, we used major element compositions of the tephra samples (dots in Fig. 13) and compared them with the known tephra sequence for Iceland (contour areas in Fig. 13), as described by Jennings *et al.* (2014) and Harning *et al.* (2018). We identified nine tephra layers from four different volcanic systems. V1717, V1477, and V1410 are tephras from the Bárðarbunga-Veiðivötn volcanic system from eruptions in 1717 C.E., 1477 C.E., and 1410 C.E., respectively. H1300, H3, and H4 are tephras from three eruptions of Hekla volcano in 1300 C.E., 2879 ± 34 cal. B.P., and 3826 ± 12 cal. B.P., respectively (Meara *et al.*, 2020). H3 and H4 are two of the largest Holocene eruptions in Iceland, producing large amounts of tephra. H3 is a fine-grained whitish layer up to 15 cm thick. H4 is a biphase layer (one thin white phase and one thicker gray phase) up to 5 cm thick. G780 and "G10ka series" are tephras from the Grímsvötn volcanic system. The "G10ka series" were deposited by several eruptions during a 500 yr long period between 10,400 and 9900 cal. B.P. (Óladóttir *et al.*, 2020), and they are widespread in and around the northern Atlantic from Greenland to northeastern Europe. The tephra Askja S from Askja volcano is dated 10,830 ± 57 cal. B.P. (Bronk Ramsey *et al.*, 2015) and therefore is a reliable marker for the early Holocene period. The sample ages are summarized in Table 3, and the raw data chemistry tables are in the supplemental material. Eight of the nine tephras identified are found at both of our study locations, but V1410 was found

TABLE 2
**Summary of the Birch Tree Radiocarbon Samples**

| Sample Number | Trench | Unit | Depth (cm) | Fraction Modern | ± | δ14C(‰) | ± | 14C Age (B.P.) | ± | Modeled Calibrated Age B.C.E. (±2σ) |
|---|---|---|---|---|---|---|---|---|---|---|
| 1 | T1w | Channel | 185 | 0.4626 | 0.0008 | −537.4 | 0.8 | 6195 | 15 | 5215–5058 |
| 4 | T1w | A1 | 200 | 0.4567 | 0.0008 | −543.3 | 0.8 | 6295 | 15 | 5312–5216 |
| 6 | T1w | A1 | 140 | 0.3909 | 0.0007 | −609.1 | 0.7 | 7545 | 15 | 6448–6392 |
| 7 | T1w | OR | 80 | 0.5546 | 0.0008 | −445.4 | 0.8 | 4735 | 15 | 3628–3381 |
| 8 | T1w | OR | 120 | 0.6031 | 0.0010 | −396.9 | 1.0 | 4060 | 15 | 2829–2493 |
| 9 | T1w | OR | 90 | 0.6250 | 0.0010 | −375.0 | 1.0 | 3775 | 15 | 2289–2221 |
| 11 | T1w | OR | 70 | 0.6644 | 0.0011 | −335.6 | 1.1 | 3285 | 15 | 1611–1506 |
| 12A | T1w | OR | 82 | 0.6610 | 0.0011 | −339.0 | 1.1 | 3325 | 15 | 1623–1537 |
| 12B | T1w | OR | 82 | 0.6638 | 0.0011 | −336.2 | 1.1 | 3290 | 15 | 1612–1510 |
| 15 | T1w | OR | 120 | 0.6566 | 0.0012 | −343.4 | 1.2 | 3380 | 20 | 1741–1616 |
| 16 | T1w | OR | 135 | 0.5339 | 0.0009 | −466.1 | 0.9 | 5040 | 15 | 3948–3781 |
| 18 | T1w | OR | 85 | 0.6926 | 0.0012 | −307.4 | 1.2 | 2950 | 15 | 1221–1114 |
| 19 | T1w | D6 | 57 | 0.6992 | 0.0011 | −300.8 | 1.1 | 2875 | 15 | 1089–980 |
| 21 | T1w | D5 | 45 | 0.6986 | 0.0014 | −301.4 | 1.4 | 2880 | 20 | 996–924 |
| 22 | T1w | D6 | 65 | 0.7072 | 0.0013 | −292.8 | 1.3 | 2780 | 15 | 1007–942 |
| 24 | T1w | OR | 100 | 0.6938 | 0.0011 | −306.2 | 1.1 | 2935 | 15 | 1216–1089 |
| 25 | T1w | OR | 130 | 0.6915 | 0.0011 | −308.5 | 1.1 | 2965 | 15 | 1257–1122 |
| 26 | T1w | D4 | 115 | 0.7338 | 0.0012 | −266.2 | 1.2 | 2485 | 15 | 769–581 |
| 27 | T1w | D4 | 65 | 0.7369 | 0.0016 | −263.1 | 1.6 | 2450 | 20 | 756–612 |
| 28 | T1w | D4 | 57 | 0.7384 | 0.0013 | −261.6 | 1.3 | 2435 | 15 | 746–646 |
| 30 | T1w | D3 | 50 | 0.7547 | 0.0012 | −245.3 | 1.2 | 2260 | 15 | 383–209 |
| 31 | T1w | Colluvial wedge | 62 | 0.7483 | 0.0012 | −251.7 | 1.2 | 2330 | 15 | 408–386 |
| 32 | T1w | Shear zone | 80 | 0.7381 | 0.0012 | −261.9 | 1.2 | 2440 | 15 | 661–412 |
| 33 | T1w | Shear zone | 110 | 0.7390 | 0.0012 | −261.0 | 1.2 | 2430 | 15 | 544–413 |
| 34 | T1w | Shear zone | 180 | 0.7343 | 0.0013 | −265.7 | 1.3 | 2480 | 15 | 670–481 |
| 35 | T1w | Shear zone | 150 | 0.7379 | 0.0012 | −262.1 | 1.2 | 2440 | 15 | 661–412 |
| 201 | T1e | A1 | 190 | 0.4585 | 0.0007 | −541.5 | 0.7 | 6265 | 15 | 5306–5211 |
| 202 | T1e | A1 | 185 | 0.4601 | 0.0007 | −539.9 | 0.7 | 6235 | 15 | 5301–5072 |
| 205 | T1e | A1 | 190 | 0.3899 | 0.0007 | −610.1 | 0.7 | 7565 | 15 | 6458–6405 |
| 206 | T1e | OR | 57 | 0.5987 | 0.0013 | −401.3 | 1.3 | 4120 | 20 | 2863–2580 |
| 207 | T1e | OR | 90 | 0.5509 | 0.0009 | −449.1 | 0.9 | 4790 | 15 | 3637–3527 |

Mass spectroscopy measurements were made at the Keck carbon cycle AMS facility, Earth System Science department at the University of California, Irvine. Ages were calibrated jointly using OxCal 4.4 (Bronk Ramsey, 2009) and calibration curve IntCal20 (Reimer *et al.*, 2020). Radiocarbon concentrations are given as fractions of the Modern standard, 14C, and conventional radiocarbon age, following the conventions of Stuiver and Polach (1977). Sample preparation backgrounds have been subtracted based on measurements of 14C-free wood. All the results have been corrected for isotopic fractionation according to the conventions of Stuiver and Polach (1977), with δ13C values measured on prepared graphite using the AMS spectrometer. These can differ from δ13C of the original material and are not shown.

only in Vestari-Krubbsskál. The tephras V1717, V1477, and G780 were not found in the Tr1 trench in Traðargerði but in trench Tr7. Similarly, the Askja S tephra was not observed in the VK1 trench in Vestari-Krubbsskál but in trench VK3. The VK1 trench in Vestari-Krubbsskál has the most complete record of tephras, because the pull-apart basin has a higher sedimentation rate. The presence at both locations of Askja S—the early Holocene tephra—confirms that the trenches span most of the Holocene period. All the tephras identified at both the locations are well documented in Iceland and have known calibrated radiocarbon ages independent from this study.

We modeled our chronological sequence using OxCal (Bronk Ramsey, 2009) integrating in stratigraphic order of the radiocarbon samples, the tephra samples, and the identified earthquakes (Fig. 14). The depths of the samples were not used to model the ages to avoid artifacts in the model due to vertical motion. The start of the sequence is defined by the tephra Askja S (bottom of the trench), and the end of the sequence is defined by the event E9 (top of the trench). We defined eight phases to group some of the radiocarbon samples according to their stratigraphy and calculate the likelihood distribution for each radiocarbon sample. Tephras were introduced in the model either as a single date when available (e.g., V1717 is dated 1717 C.E.) or as a uniform probability density function (PDF) distribution specified by the minimum and the maximum age (e.g., Hekla 3 ranges between 2950 and 3080 cal. B.P.).

## RESULTS

We correlate the trenches in Traðargerði with the trenches in Vestari-Krubbsskál using known tephras as anchors. Based on that correlation we assume that the earthquakes located between known tephras are the same in both the trenches.

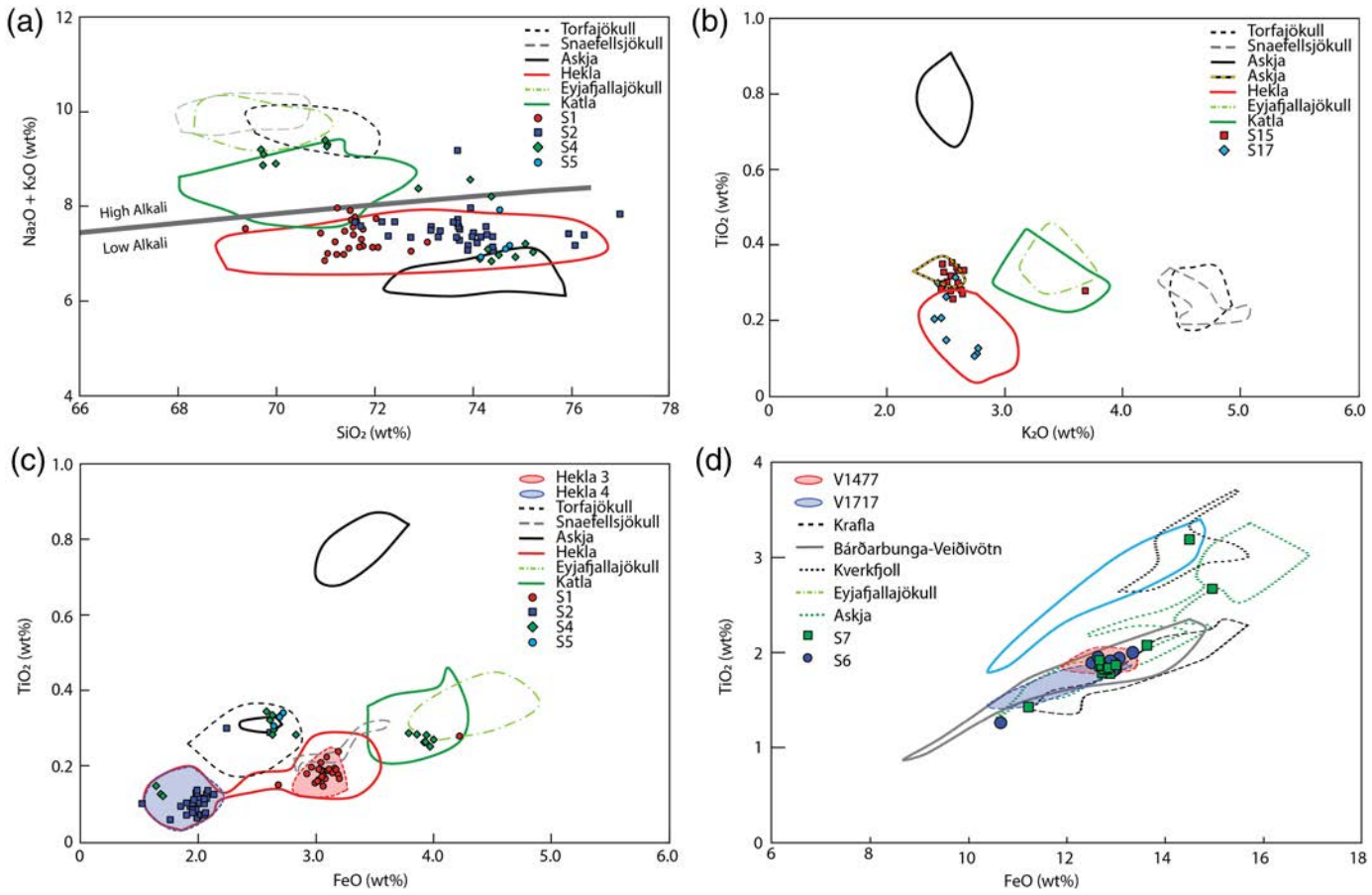


**Figure 13.** Examples of bivariate plots of major elements to identify the sources of tephra layers. The contour areas correspond to the distribution of major elements for known and documented volcanic eruptions (Jennings *et al.*, 2014; Harning *et al.*, 2018). The distribution of our measurements in these bivariate plots allows us to associate a given sample to a specific volcanic eruption. For instance, plotting (a) $Na_2O + K_2O$ as a function of $SiO_2$ and (b) $TiO_2$ as a function of $K_2O$ allow us to distinguish between the following volcanic systems of the tephra: Torfajökull, Snaefellsjökull, Askja, Hekla, Eyjafjallajökull, and Katla. Plotting FeO and $TiO_2$ allows us to identify different eruptions from the same volcanic system, for example, (c) H3 and H4 from Hekla or (d) V1477 and V1717 from the Bárðarbunga-Veidivötn volcanic system. The color version of this figure is available only in the electronic edition.

This assumption is based on the proximity of the two trench sites, the stratigraphic order of the events, and the presence of only one or two events between known tephras. The key tephras used to correlate the two sites are Askja S, Hekla 4, Hekla 3, and H1300, as all four were identified at both the locations (see stratigraphic logs in Figs. 4, 8). In Tr1 in Traðargerði, the Askja S tephra is visible at the bottom of the trench embedded in layer A2 around marks 10 and 11 (Fig. 4). Askja S is not visible at the bottom of VK1 in Vestari-Krubbsskál, probably because VK1 is not deep enough. However, Askja S is found at the bottom of VK3 in Vestari-Krubbsskál just below the unit A of sand and clay layers (see supplemental material). Unit A is found in VK1 and VK3. The uppermost datable layer found in Tr1 is H1300—a tephra produced by a one-year-long eruption of Hekla volcano in 1300 B.C.E. H1300 is also observed in VK1 but is not the uppermost tephra found in VK1. H1300 in VK1 is located 30–40 cm below the surface. In the trench VK1, we could find the tephras V1477 and V1717 above H1300 (Fig. 8)—two tephras produced by eruptions of the Bárðarbunga-Veidivötn volcanic system in 1477 C.E. and 1717 C.E., respectively. This suggests that the record of tephra layers in Vestari-Krubbsskál is more complete or at least of higher resolution than the record in Traðargerði. The presence of Askja S at the bottom and H1300 at the top in both the sites indicates that the two trench sites span most of the Holocene period.

We identified nine events in total (Figs. 14 and 15). Combining radiocarbon dating and tephrochronology allows us to obtain reliable age constraints for each earthquake. Four events are identified at both the locations: E1, E2, E3, and E5. Three events are only visible in Traðargerði, E4, E6, and E7, whereas two events are only observed in Vestari-Krubbsskál E8 and E9. The event horizon for E1 is located above unit B1, somewhere within the unit OR around mark 6, and below the rotated triangular block around mark 5 (Fig. 4). Unit B1 is not dated, but unit OR just above the event horizon of E1 is constrained by samples 7 and 207 (Fig. 4, Table 2), and the unit just below the event horizon of E1 at

mark 5 is constrained by sample 16. We constrain an age of 3575–3905 cal. B.C.E. for E1. E2 does not have a clear event horizon. However, the upward terminations of E2 in the stratigraphy are located above samples 7 and 8 but below sample 9 and tephra H4. Therefore, we constrain and age of 2264–2593 cal. B.C.E. for E2. Event E3 offsets the H4 tephra, providing a solid lower age for the event. The event horizon for E3 is a thin, black layer located few centimeters above H4 (Fig. 4). The upper age constraint is given by samples 11 and 12 just above the event horizon of E3, resulting in an age of 1669–2229 cal. B.C.E. for E3. Event E4 does not have a clear event horizon. However, the upward terminations of the faults associated with E4 are well bracketed between samples 11 and 12 below and samples 18 and 24 above, constraining an age of 1192–1535 cal. B.C.E. for E4. The event horizon for E5 is the top of H3 layer, providing a strong lower age limit. Samples 19 and 22 just above the tephra H3 constrain the upper age limit, yielding an age of 1010–1120 cal. B.C.E. for event E5. Event E6 disturbs layers D6 and D5 and most probably layer D4 (samples 26–28). In addition, E6 probably opened a ~50 cm wide fissure between F8 and F9, likely filled with sediments shortly after (samples 32–35). Finally, E6 is sealed by a colluvial wedge shortly after (sample 31). Therefore, we constrain an age of 542–714 cal. B.C.E. for E6. The faults associated with event E7 end in the unit D3 constrained by sample 30. In addition, E7 occurred after the deposition of the colluvial wedge formed after E6 and dated by sample 31 (light gray surface in Fig. 4). These constraints give an age of 250–401 cal. B.C.E. for E7. E8 is the penultimate event. Its event horizon lies between the tephras V1477 and V1717, dating the event between 1482 and 1713 C.E. Event E9 is the most recent event observed in our trenches, and it postdates the deposition of the tephra V1717 in 1717 C.E. An additional event, "event a," is only visible in Vestari-Krubbsskál (Fig. 12), but this event is not well constrained in time, assumed to be sometime after the deposition of Askja S, therefore, after 10.8 ka cal. B.P. Figure 15 summarizes the earthquake history for the HFF during the Holocene period.

We did not find evidence of events E6 and E7 in VK1. E6 and E7 ages in Tr1 are 542–714 cal B.C.E. and 250–401 cal. B.C.E., respectively (Fig. 15). Event E8 and E9 in VK1 occurred after the deposition of the tephra V1477; therefore, E8 and E9 in VK1 are not the same events as E6 and E7 in Tr1. In addition, we did not find evidence of events above the tephra layer H1300 (1300 C.E.) in Tr1. We did not observe evidence of events E8 and E9 in Tr1. For events observed in Traðargerði but not in Vestari-Krubbsskál such as E6 and E7, it is possible to assume that a rupture coming from offshore (from west) could stop between the two sites located 5 km apart.

## DISCUSSION

The deepest in situ radiocarbon samples are in the unit A1 at the bottom of Tr1, just above the gravel base (supposedly of glacial or early postglacial age), about 2 m deep, and yield an age of 5312–5058 cal. B.C.E. (samples 1 and 4, Table 2). The unit A2 is located below the unit A1 in stratigraphic order and is dated at 10.8 ka cal. B.P. from the presence of the Askja S tephra. These ages suggest that about 3 ka of sediment record may be missing in Tr1 from ~10 to ~7 ka cal. B.P. Therefore, despite the fact that Tr1 spans the entire Holocene period, the paleoseismic record before ~5000 B.C.E is missing in the trench. This lack of sediments is also supported by the erosional unconformity on top of units A (dashed blue line in Fig. 4). The presence of a reworked tephra (identified as a mix of Grímsvötn tephra and Askja S, sample S4 in Table 3) at the top of unit A2 suggests that this unconformity occurred sometime around 10 ka cal. B.P. Similarly, the U-shaped channel observed at the bottom of Tr1 from marks 7 to 9 suggests water flowing at this location and probably eroding the layers. The deepest part of the channel is dated at ~7 ka cal. B.P. (sample 1 in Table 2). A less sharp yet similar erosional unconformity is seen in Vestari-Krubbsskál on top of the lacustrine unit A (Fig. 8). The Early Preboreal period (11.5–10.1 ka cal. B.P.) marks the transition from colder to warmer periods and is usually considered as the beginning of the Holocene (Ingólfsson *et al.*, 2010). The peak deglaciation occurred between 10 and 8 ka cal. B.P. characterized by high erosion of the landscape (Norddahl *et al.*, 2008). The early Holocene period in Iceland is marked by massive glacial outburst floods caused by the catastrophic drainage of glacier lakes or pooled glacier meltwater (jökulhlaups) and causing drastic erosion of the landscape (Waitt, 2002; Wells *et al.*, 2022). Although our trench locations are not directly in glacial valleys, it is not unlikely that similar events of smaller magnitude occurred during the deglaciation period were responsible for the missing records. In fact, Holocene sedimentary deposits of glacial and fluvioglacial origin are found in and around Húsavík (Waltl *et al.*, 2018), attesting of the proximity of glaciers. In addition, well-developed vegetation cover during the Early Birch Period (9–7 ka cal. B.P.) could have limited sediment transport. This may suggest that some of the earthquake record is missing for that period.

Thorgeirsson (2011) compiled information from letters, annals, church accounts, newspapers, diaries, and travel books to produce a catalogue of historical earthquakes in North Iceland since the settlement of the island in the ninth century until the early twentieth century. Five significant earthquakes are reported in the TFZ in 1260, 1584, 1755 1838, and 1872. Almost no information and descriptions are available for the 1260 and 1584 events. The 1755 earthquake occurred on 11 September and was widely felt in North Iceland. The description of 1755 mentions that four houses collapsed on Flatey island and seven or eight houses collapsed in Húsavík, as well as the church of the town. Houses were damaged on Grímsey island, and boats were overturned near the shore of Húsavík, causing loss of life. The 1872 earthquake occurred on 18 April

TABLE 3
**Summary of the 33 Tephra Samples and the Different Volcanic Systems or Volcanic Eruptions behind Each Tephra Deposit and Their Associated Ages**

| Trench | Sample | Volcanic System | Event | Age | Reference |
|---|---|---|---|---|---|
| Tr7—N wall | S1 | Hekla | H3 | 3,080–2,950 cal B.P. ± 1$\sigma$ | Larsen *et al.* (2002) |
| Tr7—N wall | S2 | Hekla | H4 | 4,287–4,153 cal B.P. ± 2$\sigma$ | Dugmore *et al.* (1995) |
| Tr7—N wall | S3 | Askja | – | 6,750 B.P. | * |
| Tr7—N wall | S4 | Reworked Katla, Askja and Grímsvötn | Askja S/G10 ka series | 10,500–11,000 B.P. | Bronk Ramsey *et al.* (2015), Óladóttir *et al.* (2020) |
| Tr7—N wall | S5 | Askja, Grimvötn | Askja S? | 10,000–11,000 B.P. | Bronk Ramsey *et al.* (2015) |
| Tr7—S wall | S6 | Bárðarbunga-Veidivötn | V1717 | 1,717 C.E. 30 | Eiríksson *et al.* (2004) |
| Tr7—S wall | S7 | Bárðarbunga-Veidivötn | V1477 | 1,477 C.E. | Larsen *et al.* (2002) |
| Tr7—S wall | S8 | Hekla | H1300 | 1,300 C.E. | Larsen *et al.* (2002) |
| Tr7—S wall | S9 | Hekla | H3 | 3,080–2,950 cal B.P. ± 1$\sigma$ | Larsen *et al.* (2002) |
| Tr7—S wall | S10 | Hekla | H4 | 4,287–4,153 cal B.P. ± 2$\sigma$ | Dugmore *et al.* (1995) |
| Tr7—S wall | S11 | Reworked Askja and Hekla | – | 3,000–4,000 B.P. 31 | Hartley *et al.* (2016), Meara *et al.* (2020) |
| Tr7—S wall | S12 | Hekla | H4 | 4,287–4,153 cal B.P. ± 2$\sigma$ | Dugmore *et al.* (1995) |
| Tr7—S wall | S13 | Hekla | H4 | 4,287–4,153 cal B.P. ± 2$\sigma$ | Dugmore *et al.* (1995) |
| Tr1—W wall | S14 | Grímsvötn | G10ka series | 10,400–9,900 cal B.P. | Óladóttir *et al.* (2020) |
| Tr1—W wall | S15 | Askja | Askja S | 10,830 ± 57 cal B.P. ± 1$\sigma$ | Bronk Ramsey *et al.* (2015) |
| Tr1—W wall | S16 | Askja | Askja S? | 10,830 ± 57 cal B.P. ± 1$\sigma$ | Bronk Ramsey *et al.* (2015) |
| Tr1—W wall | S17 | Hekla | H1300 | 1,300 C.E. | Larsen *et al.* (2002) |
| VK1 | SK1 | Bárðarbunga-Veidivötn | V1477 | 1,477 C.E. | Larsen *et al.* (2002) |
| VK1 | SK2 | Bárðarbunga-Veidivötn | V1410? | 1,410 C.E. | Larsen *et al.* (2002) |
| VK1 | SK3 | Hekla | H1300 | 1,300 C.E. | Larsen *et al.*, 2002 |
| VK1 | SK4 | Hekla | H3 | 3,080–2,950 cal B.P. ± 1$\sigma$ | Larsen *et al.*, 2002 |
| VK1 | SK5 | Hekla | H4 | 4,287–4,153 cal B.P. ± 2$\sigma$ | Dugmore *et al.* (1995) |
| VK3 | SK6 | Grímsvötn | G10 ka series? | 10,400–9,900 cal B.P. | Óladóttir *et al.* (2020) |
| VK3 | SK7 | Askja | Askja | 10,830 ± 57 cal B.P. ± 1$\sigma$ | Bronk Ramsey *et al.* (2015) |
| VK4 | SK8 | Bárðarbunga-Veidivötn | V1717 | 1,717 C.E. | Eiríksson *et al.* (2004) |
| VK4 | SK9 | Bárðarbunga-Veidivötn | V1477 | 1,477 C.E. | Larsen *et al.* (2002) |
| VK4 | SK10 | Hekla | H1300 | 1,300 C.E. | Larsen *et al.* (2002) |
| VK4 | SK11 | Katla | Unidentified | – | – |
| VK4 | SK12 | Hekla | H3 | 3,080–2,950 cal B.P. ± 1$\sigma$ | Larsen *et al.* (2002) |
| VK4 | SK13 | Bárðarbunga-Veidivötn | Unidentified | – | – |
| VK4 | SK14 | Hekla | H4—dark part | 4,287–4,153 cal B.P. ± 2$\sigma$ | Dugmore *et al.* (1995) |
| VK4 | SK15 | Hekla | H4 - light part | 4,287–4153 cal B.P. ± 2$\sigma$ | Dugmore *et al.* (1995) |
| VK4 | SK16 | Hekla | H4 - light part | 4,287–4,153 cal B.P. ± 2$\sigma$ | Dugmore *et al.* (1995) |

*The inferred age of S3 is based on the unpublished extensive database of icelandic tephras from Thorvaldur Thorðarson, from the University of Iceland. This sample is not used in this study and is listed here for completeness of the tephra sample collection.

and is reported as two main events about one hour apart. The report mentions that most houses in Húsavík collapsed; some were moved away from their foundations and all of them were damaged. Numerous ruptures and cracks are reported from Laugardalur to Húsavíkurfjall (Fig. 2), as well as hot water and steam coming out of the cracks. The report states that the first earthquake was felt stronger close to Húsavík, whereas the second one was felt stronger on Flatey island, suggesting that the first event ruptured a fault section on the eastern side of Skjálfandi bay, whereas the second one ruptured a fault section on the western side of the bay. The 1872 earthquakes and most likely the 1755 earthquake are located on the central or eastern sections of the HFF, whereas the events in 1260, 1584, and 1838 likely occurred on the offshore section of the HFF, or elsewhere in the TFZ, based on reports (Thorgeirsson, 2011) and intensities (Halldórsson, 2005). No evidence of 1755 and 1872 was found in Tr1, Sæmundsson and Karson (2006) reports almost no deformation associated with 1755 and 1872 in trenches close to the shore, and we observed only minor disturbances in VK1 for events E8 and E9 (Fig. 15). This lack of deformation for 1755 and 1872 highlights the fact that historical accounts have to be critically interpreted and suggests that these earthquakes did not occur on the eastern part of the HFF, that is, the inland section of the fault, or may be of smaller magnitudes than previously suggested. However, it is also possible that 1755 and 1872 occurred mostly offshore, and therefore the deformation onshore in our trenches is limited.

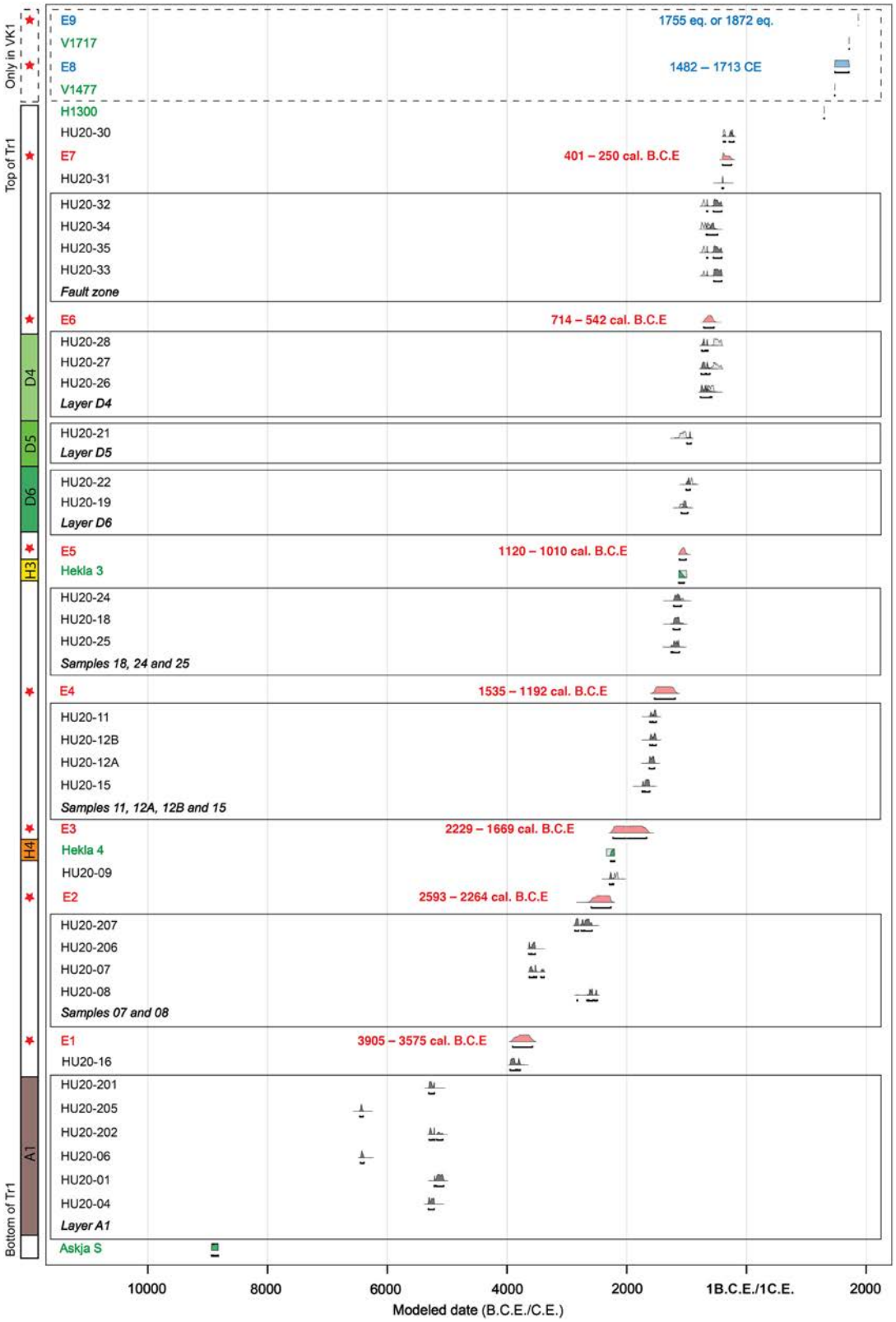


**Figure 14.** Modeled ages of 31 radiocarbon samples (in black), six tephra layers (in green), and the nine seismic events identified in the trenches (in blue, only in VK1; in red, only in Tr1 or in Tr1 and VK1). The colors on the left correspond to the stratigraphic units of Tr1 shown in Figure 4. All the samples are in stratigraphic order. The model was computed with with OxCal v.4.4 (Bronk Ramsey, 2009) and calibration curve IntCal20 (Reimer *et al.*, 2020). The color version of this figure is available only in the electronic edition.

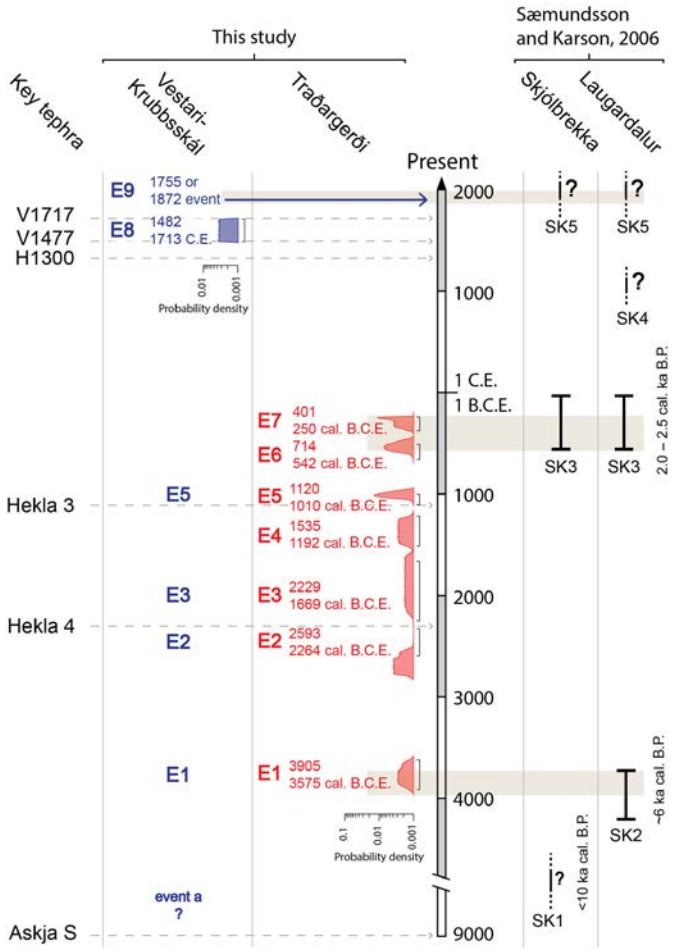


**Figure 15.** Temporal distribution of the past earthquakes on the HFF. The events E1–E9 are from the trenches Tr1 (in red) and VK1 (in blue), and are represented by their age probability density functions (PDFs) from our age model (Fig. 14) generated with OxCal. The events SK1–SK5 are the disturbances identified by Sæmundsson and Karson (2006). The color version of this figure is available only in the electronic edition.

The coseismic vertical deformation observed in our trenches is minor and ranges from 1 to 12 cm (Table 1). This vertical deformation is secondary deformation and probably does not directly scale with the magnitude of the earthquake, because the ruptures are dominated by strike slip. Nonetheless, the range of deformation suggests some variability in rupture size and magnitude. The events E5 and E7 have the largest deformation observed (4–12 cm and 4–10 cm of vertical displacement, respectively), and are associated with several faults and cracks. In addition, the significant change of thickness of the layer H3 associated with the event E5 suggests substantial horizontal slip (Fig. 5). Conversely, events E8 or E9 are only visible in Vestari-Krubbsskál and are each associated with a single crack. Moreover, E8 and E9 show limited vertical deformation (2–3 cm), hence suggesting smaller ruptures at this location. These differences in the vertical deformation suggest that events E5 or E7 were significantly larger than events E8 or E9. However, we cannot rule out the possibility that some deformation occurred on fault splays that were not sampled by our trenches.

The most recent event E9 and the penultimate event E8 are observed only in Vestari-Krubbsskál, probably because the sedimentary units and tephra layers recorded in Vestari-Krubbsskál are more complete and detailed, especially at the top part of the trench, allowing for a better temporal resolution. The penultimate event E8 occurred between 1477 and 1717 C.E. One earthquake is reported in this period, in 1584 (Thorgeirsson, 2011). The deformation associated with the event E8 may be related to the 1584 earthquake, although almost no historical information is available about this earthquake. Reports of damage (Thorgeirsson, 2011) suggest that this event may have occurred somewhere between Skagafjörður and Eyjafjörður along the western section of the HFF (Figs. 1, 16), but its location is uncertain. The most recent event E9 postdates 1717 C.E. Two significant historical earthquakes occurred after 1717 C.E., in 1755 and 1872, but we cannot discriminate between them in VK1. However, the 1755 event is usually identified as the largest earthquake of the past 270 yr on the HFF (M 7, Halldórsson, 2005), making it a potential candidate for the most recent event E9. Little to no displacement is associated with the event E9 in VK1, highlighted only by one crack, and E9 is not observed in Tr1. Similarly, Sæmundsson and Karson (2006) report little to no deformation related to the earthquakes of 1755 or 1872 on Laugardalur fault section (Fig. 2), suggesting somewhat moderate-magnitude earthquakes, possibly smaller than commonly reported (M 7 and M 6.5, respectively). However, a continuous surface rupture was observed from Laugardalur to Húsavíkurfjall (Fig. 2) after the 1872 earthquake, with reported rupture widths of 30 cm to 1 m (Thorgeirsson, 2011). Such large deformation for 1872 is not supported by our observations, as we do not identify significant deformation after the deposition of the tephra V1717 in Tr1 (Fig. 4). Similarly, Sæmundsson and Karson (2006) report only minor disturbance possibly associated with the 1755 or 1872 event on the Laugardalur fault section and did not observe any deformation on the Skjólbrekka fault section, suggesting that it did not rupture during these events. The reported deformation may have been due to liquefaction-induced lateral spreading, which can occur on gently sloping saturated soils and can displace the superficial soil above the liquefied layer by few meters (Cubrinovski and Robinson, 2016). We observed liquefaction features in Vestari-Krubbsskál (see supplemental material) but not in Traðargerði. However, tephra layers are prone to liquefaction when saturated (Youd and Perkins, 1987). In addition, the report from Thorgeirsson (2011) mentions that "whole pieces of soil and turf can be seen laying on the ground, as they had been thrown out of the crack." Blocks of mostly intact soil moved away during ground shaking are also a characteristic of lateral spreading (Youd and Garris, 1995). We observe such blocks of soil on the eastern wall of Tr1 (see supplemental material) that could have been used to backfill

the cracks after the earthquakes. In addition, the geological and geomorphological map of Húsavík shows late glacial sediments below the town (Waltl *et al.*, 2018), which are prone to earthquake-induced liquefaction. Therefore, the heavy damage and the wide cracks opened in Húsavík in 1872 could be explained by liquefaction-induced phenomena such as lateral spreading and shaking amplification. Moreover, the thin seismogenic zone of the HFF (5–10 km, Metzger and Jónsson, 2014; Abril and Gudmundsson, 2018) implies that earthquakes are shallow, therefore probably generating strong shaking that can produce significant damage even for earthquakes of moderate magnitudes (e.g., the 2016 Central Italy earthquake sequence, the two mainshocks $M_w$ 6.2 and 6.6 with hypocentral depths of 8 and 7 km, respectively, and Mercalli–Cancani–Sieberg intensities of 10–11 and the maximum peak ground acceleration of 0.4–0.5*g*, Galli *et al.*, 2017).

Intensity studies suggest that 1755 was a magnitude M ~7 event rupturing a 30–35 km long fault section from Húsavík to Flatey island (Halldórsson, 2005). Similarly, based on microseismicity, Stefánsson *et al.* (2008) estimated a 40 km long fault plane for the 1755 earthquake. Studies show that the Young's modulus in volcanic environment such as Iceland is likely two to three times lower than the commonly used 30 GPa (Sigmundsson *et al.*, 2020) due to factors like heat or fracture density (Heap *et al.*, 2020), hence yielding lower magnitudes for a given set of fault dimensions and coseismic displacement. For example, the fault parameters of the 1755 earthquake (M ~7 and fault length ~35 km) and a lower Young's modulus (10–15 GPa) would yield unrealisticly high average coseismic displacements ranging from 6 to 11 m, therefore suggesting that the rupturing fault section was longer or that the magnitude of the earthquake was lower. Similarly, following moment and moment magnitude relationships (Aki, 1966; Hanks Kanamori, 1979) for a normal crust (i.e., Young's modulus of 30 GPa), this would require a coseismic slip of 3–4 m. Such a large fault offset is unlikely from our observations in the trenches; our trenches are located just beyond the inferred rupturing section of the 1755 earthquake. This suggests that the 1755 rupture extended further offshore to the west, or the magnitude of the earthquake was smaller than M 7. However, we cannot exclude that some of the Holocene deformation occurred on other fault strands. For example, Sæmundsson and Karson (2006) reported vertical displacement on the Skjólbrekka fault section just north of the Laugardalur fault section where our trench site of Traðargerði is located, suggesting that deformation occurred on this fault section during the Holocene. However, the Skjólbrekka fault section itself is 3 km long and up to 7 km long, including the inferred offshore section. Therefore, the Skjólbrekka fault is most likely too short to generate large earthquake, but it is possible that some slip occurred on the Skjólbrekka during an event rupturing the Laugardalur fault section.

Sæmundsson and Karson (2006) excavated four paleoseismic trenches covering the Holocene period on the Skjólbrekka and Laugardalur fault sections, north of Húsavík (Fig. 2) and interpreted stratigraphic disturbances and debris slides as markers of seismic events. The chronology of the events is based only on six sparse tephra layers spanning 10 ka (V1717, V1477, H3, H4, Saksunarvatn, and Askja S); therefore, the age constraints are not strong. They report five disturbances most likely associated with faulting events (SK1–SK5 in Fig. 15): two 8
on the Skjólbrekka fault (SK1 and SK3) and four on Laugardalur fault where our trench Tr1 is located (SK2–SK5). They observe the two largest disturbances in early Holocene and around 2.5 ka cal. B.P. (SK1 and SK3 in Fig. 15, respectively). We tentatively associate our events E1, E6/E7, and E9 9
with the events SK2, SK3, and SK5, respectively. SK3 overlaps in time with both E6 and E7, suggesting that one of these two events is the same as SK3. Sæmundsson and Karson (2006) observe two smaller disturbances around 6 ka cal. B.P. and 1000 C.E. (SK2 and SK4 in Fig. 15, respectively). The timing of SK2 around 6 ka cal. B.P. suggests that the SK2 corresponds to our event E1. Finally, the most recent event SK5 most probably corresponds to the one of the most recent events in 1755 or 1872. Sæmundsson and Karson (2006) report little to no displacement for the historical events in 1755 and 1872 (SK5 in Fig. 15). Even though Sæmundsson and Karson (2006) note that their study should not be taken as a complete record of past earthquakes, the lack of large and sharp deformation in the subsurface suggests that not many large, surface-rupturing earthquakes occurred during Holocene.

The base of the seismogenic zone on oceanic transform fault is characterized by the 600°C isotherm (Abercrombie and Ekstrom, 2001; Boettcher and McGuire, 2009). In northern Iceland, the geothermal gradient decreases from 70° to 80°C/km on the western Tjörnes peninsula, close to the NVZ, to 60°C/km in the Skjálfandi bay and decreases further westward (Flóvenz and Sæmundsson, 1993). This suggests a very thin seismogenic layer to the east (7–8 km deep) that thickens toward the west to 10–12 km as we go away from the rift. This range of seismogenic depths is in agreement with results from inversions of geodetic data that also suggest a locking depth of 6–10 km along the HFF (Metzger and Jónsson, 2014). In addition, the relocation of earthquakes in northern Iceland also indicates seismogenic depths of 5–10 km but shallowing westward (Abril and Gudmundsson, 2018). The authors explain this by the transition from the thin Icelandic seismogenic crust in the east to a more typical, thicker, oceanic crust in the west. Despite its shallowness, however, it would produce an earthquake of magnitude M ~7.2–7.3 if the entire seismogenic crust along the HFF would rupture.

If we consider only the last two earthquakes in 1755 and 1872, we can presume a return time of ~120 yr for large earthquakes (M 6.5–7). However, we do not see evidence for large deformation for 1755 and 1872 in our trenches, and we review next why we assume they are not among the largest earthquakes on the HFF. In the following, we considered five

sequences of earthquakes: E2–E7 (optimal subset of our catalog), E1–E9 (our entire catalog), E2–E9 including SK4, E1–E9 including SK4, and our catalog excluding the lowest ranked events E2 and E4 and including SK4, and calculated the coefficient of variation (CV) of return times for each sequence (Parsons, 2008; Styron, 2019). For the sequence E2–E7, the average return time is 421 yr, and the standard deviation of the return times is 122 yr, yielding a CV of 0.29. For the sequence E1–E9, the average return time is 694 yr, and the standard deviation of the return times is 604 yr, giving a CV of 0.87. In that case, the average return time is strongly affected by the gaps between E1 and E2 and between E7 and E8, reflected in the high standard deviation. In fact, for the sequence E1–E9 including SK4, the average return time is 548 yr, and the standard deviation is 335 yr, yielding a CV of 0.61. In that case, including the event SK4 between E7 and E8 lowers the average return time and decreases the standard deviation. The sequence E2–E9 including SK4 has an average return time of 452 yr and a standard deviation of 187, giving a CV of 0.41. Finally, for the catalog excluding the lower ranked events E2 and E4, we calculated an average return time of 793 yr and a standard deviation of return times of 604 yr, yielding a CV of 0.76. In these five cases, the CV is lower than 1, therefore suggesting quasi-periodic earthquakes (Styron, 2019) even though the sequence E1–E9 and the sequence without lower ranked events have a CV of 0.87 and 0.76, respectively, close to 1, suggested some randomness in the earthquake return times.

Considering the sequence E1–E9 including SK4, our catalog of the past earthquakes suggests a return time around 550 yr (Fig. 15), significantly longer than 120 yr. A slip rate of 6–9 mm/yr (Metzger and Jónsson, 2014) and a return time of ~550 yr imply a slip accumulation of 3–4.5 m corresponding to an earthquake of magnitude 7.2–7.3 rupturing the entire fault length (Aki, 1966; Hanks and Kanamori, 1979), assuming all the seismic moment was released in the last large earthquake and steady moment accumulation since then. However, this scenario does not account for more frequent moderate earthquakes (i.e., M 6.5+ every ~120 yr) such as the 1755 and 1872 earthquakes. For a slip rate of 6–9 mm/yr and a return time of 120 yr for moderate earthquake, we calculate a slip accumulation of 0.9 ± 0.2 m. This amount of slip corresponds to an earthquake of magnitude M 6.7, rupturing a 50 km long and 6–10 km wide fault section. Four earthquakes of magnitude M 6.7 in ~550 yr represent about 50% of the total seismic moment accumulated in ~420 yr. The remaining 50% of seismic moment correspond to an earthquake of magnitude M 7.0–7.1, rupturing the entire fault length of the HFF with an average coseismic slip of 2 m. Therefore, we suggest that large earthquakes occur every ~550 yr on the HFF, and we propose that the historical earthquake record based on intensities and reports (Thorgeirsson, 2011), such as the events in 1755 or 1872, were not amongst the largest earthquakes occurring on the fault.

The expected seismic moment accumulated on the fault over ~6000 yr, considering a slip rate of 6–9 mm/yr, a fault length and width of 100 km and 6–9 km, respectively, and a Young's modulus of 15–30 GPa, ranges from $3.2 \times 10^{20}$ N · m to $14.6 \times 10^{20}$ N · m. In comparison, the cumulative estimated seismic moment released by the nine earthquakes from our catalog in the last ~6000 yr, considering a coseismic slip of 2–3 m, a fault length and width of 100 km and 6–9 km, respectively, and a Young's modulus of 15–30 GPa, ranges from $1.6 \times 10^{20}$ N · m to $7.3 \times 10^{20}$ N · m, about half of what would be expected from the slip rate. This amount of seismic moment "missing" could be accommodated by aseismic slip or seismic swarms that have been inferred on oceanic transform faults (Boettcher and Jordan, 2004; Roland and McGuire, 2009) and suggested on the HFF (Passarelli *et al.*, 2018). It is also possible that some earthquakes were missed in our trenches or occurred offshore, and therefore are not accounted for in this seismic moment calculation. Finally, some of the seismic moment "missing" is released by the moderate earthquakes of magnitude ~6.5.

To discuss the possible segmentation of the HFF, we used the intensities compiled in Thorgeirsson (2011), and we propose a spatial distribution for historical earthquakes in the TFZ (Fig. 16 and supplemental material). We assume that most of the large earthquakes reported in the TFZ occurred on the HFF. Earthquakes seem to be split into western earthquakes from Flatey island westwards (1584, 1838) and eastern earthquakes from Flatey island eastward (1755, 1872), suggesting a geometric complexity around Flatey island acting as a barrier to the earthquake rupture propagation (Fig. 1). At this location, a 1 km wide left step in the fault suggests the presence of a compressional jog between Flatey island and Flateyjarskagi peninsula. Similarly, the two earthquakes in 1872 seem to have ruptured first in the eastern side of Skjálfandi bay close to Húsavík and then in the western side of Skjálfandi bay close to Flatey island. The middle of the flat Skjàlfandi bay is characterized by 2 km wide left step in the fault resulting in a 30–40 m high pressure ridge. We suggest that this stepover in the fault located in the middle of Skjálfandi bay (Fig. 1b) may act as a barrier to the propagation of some earthquake ruptures. This segmentation of the fault could in part explain the rare occurrence of large earthquakes along the HFF. In addition, the eastern segment seems to produce more earthquakes than the western one. One possible explanation is that the western end of the HFF has been experiencing several earthquake swarms in the present day, suggesting significant slip and strain release (Passarelli *et al.*, 2018), therefore limiting the stress accumulation on the western part of the fault.

Oceanic transform faults have low seismic coupling—on average around 15%, with most of the slip happening aseismically or in seismic swarms (Boettcher and Jordan, 2004). In fact, aseismic stress release has been postulated on the HFF (Passarelli *et al.*, 2018), although there is no clear evidence for aseismic motion from Global Navigation Satellite Systems observations. Studies

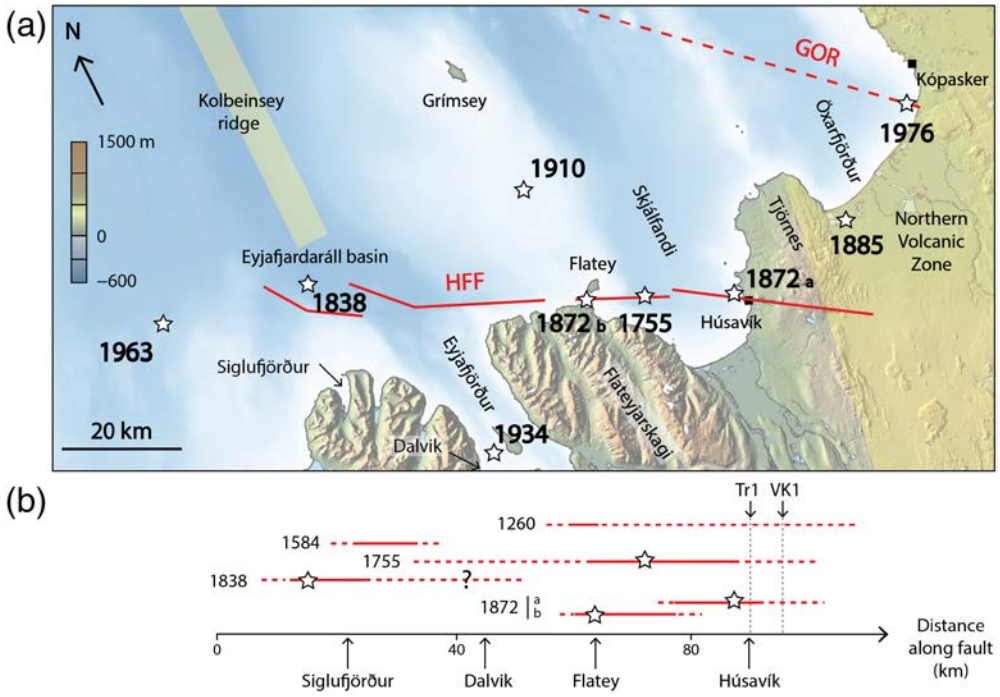


**Figure 16.** (a) Map of the TFZ for which the solid and red dashed lines represent the HFF and the Grímsey oblique rift (GOR), respectively. White stars show approximate locations of historical earthquakes. (b) The horizontal red lines represent the rupturing faults during each historical events inferred from the intensities reported in Thorgeirsson (2011). More detailed map and descriptions are available in the supplemental material. The color version of this figure is available only in the electronic edition.

based on teleseismic data show that oceanic transform faults have a quasi-periodic seismic behavior with the same fault segments rupturing regularly and geometric features stopping the rupture (Boettcher and McGuire, 2009). This behavior has been observed on fast-slipping transforms such as the Gofar transform fault, East Pacific Rise (McGuire *et al.*, 2005; McGuire, 2008), or the Blanco ridge transform (Liu *et al.*, 2020), with the maximum earthquake magnitude of M 5.4–6.4 (Boettcher and McGuire, 2009). Aderhold and Abercrombie (2016) observed a similar quasi-periodic behavior on the slow-slipping Charlie-Gibbs transform fault (~22 mm/yr), even for higher magnitudes (M ~7). The results from our trenches show that the HFF has a quasi-periodic behavior with a repeating time of earthquakes of 600 ± 200 yr. However, the fault sections that ruptured during the past earthquakes are not known. Nonetheless, our rupture map (Fig. 16) built from the historical intensities compiled by Thorgeirsson (2011) suggests that moderate earthquakes (M ~6 to 6.5+) may repeatedly rupture similar sections of the fault. Indeed, the earthquake activity on the HFF during the last 800 yr seems to alternate between the western section, west of Flatey island, and the eastern section, east of Flatey island (Fig. 16, Thorgeirsson, 2011).

Oceanic transform faults are often several hundreds of kilometers long, but large earthquakes do not occur on oceanic transform faults. The earthquake magnitudes are usually less than M ~7.5. This is explained by strong segmentation of the oceanic transform fault due to fault geometry and seismic coupling. Similar to continental strike-slip faults (Biasi and Wesnousky, 2017; Lefevre *et al.*, 2020; Jiao *et al.*, 2021), observations on oceanic transform faults show structural control on the fault segmentation for which fault bends and stepover act as barriers to the propagation of the rupture (Brothers *et al.*, 2020). In addition, some fault segments are fully coupled and rupture in a quasi-periodic behavior, whereas some fault patches are poorly coupled and characterized by aseismic slip. These poorly coupled fault patches can act as barrier to the rupture propagation, therefore limiting the maximum magnitude of the earthquakes (McGuire *et al.*, 2005; Boettcher and McGuire, 2009; Sykes and Ekstrom, 2012). We observe similar structural segmentation along the HFF, in particular, the relay zone close to Flatey island and the pressure ridge in the middle of Skjálfandi bay (Fig. 1), which may explain the rare occurrence of large earthquakes on the HFF that would require a full fault length rupture.

Earthquakes of magnitude M > 6+ occur on large oceanic transform faults such as the 2015 $M_w$ 7.1 Charlie Gibbs earthquake rupturing a ~125 km long section of a 220 km long transform fault at 15 km of depth (Aderhold and Abercrombie, 2016) or the 2016 $M_w$ 7.1 Romanche earthquake rupturing 100–120 km long section of the ~1000 km long Romanche transform fault at 15–20 km of depth (Hicks *et al.*, 2020). However, the reported return times are much shorter than what we observe in North Iceland—~30 yr on the Charlie Gibbs transform fault for M > 6.5 (Aderhold and Abercrombie, 2016) and around 4 yr on the Romanche transform fault for M > 6.5 (Hicks *et al.*, 2020). Although the faster slip rates of the Charlie Gibbs transform (~22 mm/yr) and the Romanche transform (~32 mm/yr) could explain this difference in return times, these earthquakes are partial fault ruptures. Therefore, we infer that these short return times observed on the Charlie Gibbs and Romanche transforms could correspond to the "short" cycle of moderate earthquakes on the HFF, and that these large oceanic transform faults are capable of generating significantly larger earthquakes rupturing longer fault sections and

corresponding to the "long" cycle observed in our trenches with a longer return time.

## CONCLUSIONS

Combining observations from our trenches with radiocarbon and tephra samples, we built the most complete catalog to date of moderate-to-large earthquakes in North Iceland for the Holocene period. We presented here two excavation sites—Traðargerði and Vestari Krubbsskál—along the eastern section of the HFF. We identified nine earthquakes in total, out of which four are observed at both the locations. The amplitudes of the deformation observed in the trenches are not large, suggesting that earthquakes of large magnitude are rare on the HFF. Indeed, following moment and moment magnitude relationships, we determine the maximum magnitude of 7.2–7.3 for an event rupturing the entire fault length. Based on the age constraints, we inferred a return time of 600 ± 200 yr for these events.

We associate our most recent event to one of the last major historical earthquakes in 1755, although we cannot exclude that this event actually corresponds to an historically recorded earthquake in 1872. Similar to the other events, the deformation associated with the last event suggests that 1755 either occurred mainly on the western offshore section of the fault or that the magnitude of the earthquake is smaller than that previously inferred from intensities (M ∼7, Halldórsson, 2005). Similar observations in other paleoseismological trenches suggest that the deformation from the earthquakes of 1755 and 1872 is minor on the inland section of the fault (Sæmundsson and Karson, 2006).

Our work represents the first integrated paleoseismological study of the HFF and of an oceanic transform fault. We provide a 6000 yr long earthquake catalog—the longest record of earthquake ruptures on the HFF and for an oceanic transform fault. Our catalog suggests a quasi-periodic behavior of the seismic activity, and rupture maps from intensities suggest repeated rupture fault sections similar to what is observed on oceanic transform faults (Boettcher and McGuire, 2009; Aderhold and Abercrombie, 2016). Our observations suggest that a full rupture of the fault is rare. We infer that the instrumental catalogs available for oceanic transform faults do not cover the entire seismic cycle despite suggested short return time (<30 yr), and that oceanic transform faults may produce larger earthquakes (M 7+) with longer return times.

## DATA AND RESOURCES

The large and intermediate scale digital elevation models (DEMs) are from the National Land Survey of Iceland and can be obtained from their website (https://www.lmi, last accessed September 2021). The bathymetric data are from the Icelandic Coast Guard and are provided by Ásta Rut Hjartardóttir from the University of Iceland. They cannot be released to the public. The IMO seismic catalog is from the Icelandic Meteorological Office and can be obtained from their website (https://www.vedur.is, last accessed March 2019). The small-scale digital surface model (DSM) from the Unmanned Aerial Vehicle (UAV) photographs, the trench photographs, the radiocarbon samples, and the tephra samples were collected for this study. These data are available upon request. We provide three supplemental material files: one file containing the chemistry tables of the tephra samples from Traðargerði, one file containing the chemistry tables of the tephra samples from Vestari Krubbsskál, and one file containing additional figures.

## DECLARATION OF COMPETING INTERESTS

The authors acknowledge that there are no conflicts of interest recorded.

## ACKNOWLEDGMENTS

The authors thank associate editor of *BSSA*, Thomas Brocher, and the two reviewers Katherine Scharer and Glenn Biasi for their thorough review of the article and the many helpful comments and suggestions for improving the article. This research was supported by King Abdullah University of Science and Technology (KAUST) under Award Number BAS/1/1353-01-01. This research was also supported by the Agence Nationale de la Recherche (ANR—French National Agency for Research) under the project ANR-18-C31-0012. The authors thank Gaukur Hjartarson at the Norðurthing municipality in Húsavík for granting access to the two trench sites and Bjarni Höskuldsson for allowing them to trench on the horse grazing land he uses in Traðargerði. The authors thank Daniele Trippanera, Jörg Follmann, Nico Augustin, and Froukje van der Zwan for their assistance on the field. Finally, the authors thank Jonathan Harrington for his active participation in the initiation of the project and for managing the field work in Vestari-Krubbsskàl.

## REFERENCES

Abercrombie, R. E., and G. Ekstrom (2001). Earthquake slip on oceanic transform faults, *Nature* **410,** no. 6824, 74–77.

Abril, C., and O. Gudmundsson (2018). Relocating earthquakes with empirical traveltimes, *Geophys. J. Int.* **214,** no. 3, 2098–2114.

Aderhold, K., and R. E. Abercrombie (2016). The 2015 Mw 7.1 earthquake on the Charlie-Gibbs transform fault: Repeating earthquakes and multimodal slip on a slow oceanic transform, *Geophys. Res. Lett.* **43,** no. 12, 6119–6128.

Aki, K. (1966). Generation and propagation of G waves from the Niigata earthquake of June 16, 1964, estimation of earthquake moment, released energy, and stress strain drop from the G wave spectrum, *Bull. Earthq. Res. Inst. Univ. Tokyo* **44,** no. 1, 73–88.

Biasi, G., and S. Wesnousky (2017). Bends and ends of surface ruptures, *Bull. Seismol. Soc. Am.* **107,** 2543–2560.

Boettcher, M. S., and T. H. Jordan (2004). Earthquake scaling relations for mid-ocean ridge transform faults, *J. Geophys. Res.* **109,** no. 12, 1–21.

Boettcher, M. S., and J. J. McGuire (2009). Scaling relations for seismic cycles on mid-ocean ridge transform faults, *Geophys. Res. Lett.* doi: 10.1029/2009GL040115.

Bronk Ramsey, C. (2009). OxCal: Versatile tool for developing paleoearthquake chronologies - A primer, *Seismol. Res. Lett.* **80,** no. 3, 431–434.

Bronk Ramsey, C., P. G. Albert, S. P. E. Blockley, M. Hardiman, R. A. Housley, C. S. Lane, S. Lee, I. P. Matthews, V. C. Smith, and J. J.

Lowe (2015). Improved age estimates for key Late Quaternary European tephra horizons in the RESET lattice, *Quaternary Sci. Rev.* **118,** 18–32.

14 Brothers, D. S., N. C. Miller, J. Vaughn Barrie, R. J. Haeussler, H. Gary Greene, B. D. Andrews, O. Zielke, J. Watt, and P. Dartnell (2020). Plate boundary localization, slip-rates and rupture segmentation of the Queen Charlotte Fault based on submarine tectonic geomorphology, *Earth Planet. Sci. Lett.* **530,** 115882.

Cubrinovski, M., and K. Robinson (2016). Lateral spreading: Evidence and interpretation from the 2010 2011 Christchurch earthquakes, *Soil Dynam. Earthq. Eng.* **91,** 187–201.

DeMets, C., R. G. Gordon, and D. F. Argus (2010). Geologically current plate motions, *Geophys. J. Int.* **181,** 1–80.

Dugmore, A., G. Cook, J. Shore, A. Newton, K. Edwards, and G. Larsen (1995). Radiocarbon dating tephra layers in Britain and Iceland, *Radiocarbon* **37,** 379–388.

Flóvenz, O. G., and K. Sæmundsson (1993). Heat flow and geothermal processes in Iceland, *Tectonophysics* **225,** nos. 1/2, 123–138.

Galli, P., S. Castenetto, and E. Peronace (2017). The macroseismic intensity distribution of the 30 October 2016 earthquake in Central Italy (Mw 6.6): Seismotectonic implications, *Tectonics* **36,** no. 10, 2179–2191.

Garcia, S., N. Arnaud, J. Angelier, F. Bergerat, and C. Homberg (2003). Rift jump process in Northern Iceland since 10 Ma for 40Ar/39Ar geochronology, *Earth Planet. Sci. Lett.* **214,** 529–544.

Geirsdóttir, A., M. Gifford, A. Yarrow, and S. Ólafsdóttir (2009). Holocene and latest Pleistocene climate and glacier fluctuations in Iceland, *Quaternary Sci. Rev.* **28,** 2107–2118.

Gudmundsdóttir, E. R., J. Eiriksson, and G. Larsen (2011). Identification and definition of primary and reworked tephra in Late Glacial and Holocene marine shelf sediments off North Iceland, *J. Quat. Sci.* **26,** no. 6, 589–602.

Gudmundsdóttir, E. R., G. Larsen, and J. Eiríksson (2012). Tephra stratigraphy on the North Icelandic shelf: Extending tephrochronology into marine sediments off North Iceland, *Boreas* **41,** no. 4, 719–734.

Gudmundsson, A. (2000). Dynamics of volcanic systems in Iceland: Example of tectonism and volcanism at Juxtaposed hot spot and mid-ocean ridge systems, *Annu. Rev. Earth Planet. Sci.* **28,** 107–140.

Gudmundsson, A., S. Brynjolfsson, and M. T. Jónsson (1993). Structural analysis of a transform fault-rift zone junction in North Iceland, *Tectonophysics* **220,** nos. 1/4, 205–221.

Halldórsson, P. (2005). Earthquake activity in N-Iceland (in Icelandic), *Icelandic Meteorological Office Rept. 05021*, 34–41.

Hanks, T. C., and H. Kanamori (1979). A moment magnitude scale, *J. Geophys. Res.* **84,** no. B5, 2348–2350.

Harning, D., T. Thordarson, Á. Geirsdóttir, K. Zalzal, and G. Miller (2018). Provenance, stratigraphy and chronology of Holocene tephra from Vestfirdir, Iceland, *Quat. Geochronol.* **46,** 59–76.

15 Heap, M. J., M. Villeneuve, F. Albino, J. I. Farquharson, E. Brothelande, F. Amelung, J. L. Got, and P. Baud (2020). Towards more realistic values of elastic moduli for volcano modelling, *J. Volcanol. Geotherm. Res.* **390,** 106684.

Hellqvist, M., M. Hättestrand, E. Norström, E. Almgren, J. N. Johansson, and R. Traustadóttir (2020). Environment and climate change during the late Holocene in Hjaltadalur, Skagafjórdur, northern Iceland, *Geografiska Annaler* **102,** no. 1, 68–82.

Hey, R. N. (2005). Tectonics: Propagating rifts and microplates at 16 mid-ocean ridges, in *Encylopedia of Geology*, 396–405.

Hicks, S. P., R. Okuwaki, A. Steinberg, C. A. Rychert, N. Harmon, R. E. Abercrombie, P. Bogiatzis, D. Schlaphorst, J. Zahradnik, J.-M. Kendall, *et al.* (2020). Back-propagating supershear rupture in the 2016 Mw 7.1 Romanche transform fault earthquake, *Nature Geosci.* **13,** 647–653.

Homberg, C., F. Bergerat, J. Angelier, and S. Garcia (2010). Fault interaction and stresses along broad oceanic transform zone: Tjornes fracture zone, north Iceland, *Tectonics* **29,** no. 1, doi: 10.1029/2008TC002415.

Ingólfsson, O., H. Norddahl, and A. Schomacker (2010). 4 deglaciation and Holocene glacial history of Iceland, *Develop Quat. Sci.* **13,** 51–68.

Jennings, A., T. Thordarson, K. Zalzal, J. Stoner, C. Hayward, Á. Geirsdóttir, and G. Miller (2014). Holocene tephra from Iceland and Alaska in SE Greenland shelf sediments, *Geol. Soc. Spec. Publ.* **398,** no. 1, 157–193.

Jiao, L., Y. Klinger, and L. Scholtes (2021). Fault segmentation pattern controlled by thickness of brittle crust, *Geophys. Res. Lett.* **48,** no. 19, doi: 10.1029/2021GL093390.

Jónasson, K., B. Bessason, Á. Helgadóttir, P. Einarsson, G. B. Gudmundsson, B. Brandsdóttir, K. S. Vogfjörd, and K. Jónsdóttir (2021). A harmonised instrumental earthquake catalogue for Iceland and the northern Mid Atlantic Ridge, *Nat. Hazards Earth Syst. Sci.* **21,** no. 7, 2197–2214.

Jónsdóttir, K., G. Gudmundsson, L. Passarelli, and S. Jónsson (2019). The Kopasker seismic swarm in spring 2019, *Proc. of the Northquake Workshop*, Husavik, Iceland, 21–24 May 2019, ed. fekkingarnet fingeyinga.

Kagan, Y., P. Bird, and D. Jackson (2010). Earthquake forecasting in diverse tectonic zones of the globe, *Pure Appl. Geophys.* **168,** 1–21.

Karson, J. A. (2017). The Iceland plate boundary zone: Propagating rifts, migrating transforms, and rift-parallel strike-slip faults, *Geochem. Geophys. Geosys.* **18,** no. 11, 4043–4054.

Larsen, G., and J. Eiriksson (2008). Holocene tephra archives and tephrochronology in Iceland - a brief overview, *Jokull* **58,** 229–250.

Larsen, G., J. Eiríksson, K. L. Knudsen, and J. Heinemeier (2002). Correlation of late Holocene terrestrial and marine tephra markers, north Iceland: Implications for reservoir age changes, *Polar Res.* **21,** no. 2, 283–290.

Lefevre, M., P. Souloumiac, N. Cubas, and Y. Klinger (2020). Experimental evidence for crustal control over seismic fault segmentation, *Geology* **48,** no. 8, 844–848.

Liu, Y., J. J. McGuire, and M. D. Behn (2012). Frictional behavior of oceanic transform faults and its influence on earthquake characteristics, *J. Geophys. Res.* doi: 10.1029/2011JB009025.

Liu, Y., J. J. McGuire, and M. D. Behn (2020). Aseismic transient slip on the Gofar transform fault, East Pacific Rise, *Proc. Natl. Acad. Sci. Unit. States Am.* **117,** no. 19, 10,188–10,194.

Lowe, D. J., N. J. G. Pearce, M. A. Jorgensen, S. C. Kuehn, C. A. Tryon, and C. L. Hayward (2017). Correlating tephras and cryptotephras using glass compositional analyses and numerical and statistical methods: Review and evaluation, *Quaternary Sci. Rev.* **175,** 1–44.

Maccaferri, F., E. Rivalta, L. Passarelli, and S. Jónsson (2013). The stress shadow induced by the 1975-1984 Krafla rifting episode, *J. Geophys. Res.* **118,** no. 3, 1109–1121.

Magnúsdóttir, S., and B. Brandsdóttir (2011). Tectonics of the Theistareykir fissure swarm, *Jökull*, **61,** 65–79.

Magnúsdóttir, S., B. Brandsdóttir, N. Driscoll, and R. Detrick (2015). Postglacial tectonic activity within the Skjalfandadjup Basin, Tjornes Fracture Zone, offshore Northern Iceland, based on high resolution seismic stratigraphy, *Mar. Geol.* **367,** 159–170.

McGuire, J. J. (2008). Seismic cycles and earthquake predictability on East Pacific rise transform faults, *Bull. Seismol. Soc. Am.* **98,** no. 3, 1067–1084.

McGuire, J. J., M. S. Boettcher, and T. H. Jordan (2005). Foreshock sequences and short-term earthquake predictability on East Pacific Rise transform faults, *Nature* **434,** no. 7032, 457–461.

Meara, R. H., T. H. Thórdarson, N. J. G. Pearce, C. Hayward, and G. Larsen (2020). A catalogue of major and trace element data for Icelandic Holocene silicic tephra layers, *J. Quat. Sci.* **35,** nos. 1/2, 122–142.

Metzger, S., and S. Jónsson (2014). Plate boundary deformation in North Iceland during 1992-2009 revealed by InSAR time-series analysis and GPS, *Tectonophysics* **634,** 127–138.

Mosar, J., G. Lewis, and T. H. Torsvik (2002). North Atlantic sea-floor spreading rates: Implications for the Tertiary development of inversion structures of the Norwegian-Greenland Sea, *J. Geol. Soc.* **159,** no. 5, 503–515.

17 Müller, K., J. Winsemann, M. Pisarska Jamrozy, T. Lege, T. Spies, and C. Brandes (2021). The Challenge to Distinguish Soft-Sediment Deformation Structures (SSDS) Formed by Glaciotectonic, Periglacial and Seismic Processes in a Formerly Glaciated Area: A Review and Synthesis, Cambridge University Press, 67–88.

Norddahl, H., O. Ingólfsson, H. Pétursson, and M. Hallsdóttir (2008). Late Weichselian and Holocene environmental history of Iceland, *Jokull* **58,** no. 1, 343–364.

18 Óladóttir, B. A., T. Thórdarson, A. Geirsdóttir, G. E. Jóhannsdóttir, and J. Mangerud (2020). The Saksunarvatn Ash and the G10ka series tephra. Review and current state of knowledge, *Quat. Geochronol.* **56,** 101041.

Owen, G., and M. Moretti (2008). Determining the origin of soft sediment deformation structures: A case study from Upper Carboniferous delta deposits in south west Wales, UK, *Terra Nova* **20,** no. 3, 237–245.

Parsons, T. (2008). Earthquake recurrence on the south Hayward fault is most consistent with a time dependent, renewal process, *Geophys. Res. Lett.* **35,** no. 21, doi: 10.1029/2008GL035887.

Pasquare Mariotto, F., F. L. Bonali, A. Tibaldi, D. Rust, P. Oppizzi, and A. Cavallo (2015). Holocene displacement field at an emerged oceanic transform-ridge junction: The Husavik-Flatey Fault - Gudfinnugja Fault system, North Iceland, *J. Struct. Geol.* **75,** 118–134.

Passarelli, L., E. Rivalta, S. Jónsson, M. Hensch, S. Metzger, S. S. Jakobsdóttir, F. Maccaferri, F. Corbi, and T. Dahm (2018). Scaling and spatial complementarity of tectonic earthquake swarms, *Earth Planet. Sci. Lett.* **482,** 62–70.

Reimer, P., W. Austin, E. Bard, A. Bayliss, P. Blackwell, C. Bronk Ramsey, M. Butzin, H. Cheng, R. Edwards, M. Friedrich, *et al.* (2020). The IntCal20 Northern Hemisphere radiocarbon age calibration curve, *Radiocarbon* **62,** 725–757.

Rizza, M., L. Bollinger, S. N. Sapkota, P. Tapponnier, Y. Klinger, Ç. Karakaş, E. Kali, M. Etchebes, D. R. Tiwari, I. Siwakoti, *et al.* (2019). Post earthquake aggradation processes to hide surface ruptures in thrust systems: The M 8.3, 1934, Bihar-Nepal earthquake ruptures at Charnath Khola (Eastern Nepal), *J. Geophys. Res.* **124,** no. 8, 9182–9207.

Rockwell, T. K., T. E. Dawson, J. Young Ben-Horin, and G. Seitz (2015). A 21-event, 4,000-year history of surface ruptures in the Anza Seismic Gap, San Jacinto Fault, and implications for long-term earthquake production on a major plate boundary fault, *Pure Appl. Geophys.* **172,** no. 5, 1143–1165.

Roland, E., and J. J. McGuire (2009). Earthquake swarms on transform faults, *Geophys. J. Int.* **178,** 1677–1690.

Roland, E., M. Behn, and G. Hirth (2010). Thermal-mechanical behavior of oceanic transform faults: Implications for the spatial distribution of seismicity, *Geochem. Geophys. Geosys.* **11,** doi: 10.1029/2010GC003034.

Sæmundsson, K. (1974). Evolution of the axial rifting zone in Northern Iceland and the Tjornes fracture zone, *Bull. Geol. Soc. Am.* **85,** no. 4, 495–504.

Sæmundsson, K. (2013). Nature of the Husavik Faults and Holocene 19 movement on them, *Proc. of the International Workshop on Earthquakes in North Iceland*, ed. fekkingarnet fingeyinga.

Sæmundsson, K., and J. A. Karson (2006). Stratigraphy and tectonics of the Húsavík-Western Tjornes Area, *Iceland Geosurvey Rept. ISOR2006/32*.

Sæmundsson, K., A. Hjartarson, I. Kaldal, M. A. Sigurgeirsson, S. G. Kristinsson, and S. Vikingsson (2012). Geological Map of Northern Volcanic Zone, Iceland. Northern Part. 1:100 000, *Iceland GeoSurvey and Landsvirkjun*.

Scharer, K. M., R. J. Weldon, T. E. Fumal, and G. P. Biasi (2007). Paleoearthquakes on the southern San Andreas Fault, Wrightwood, California, 3000 to 1500 B.C.: A new method for evaluating paleoseismic evidence and earthquake horizons, *Bull. Seismol. Soc. Am.* **97,** no. 4, 1054–1093.

Sclater, J. G., N. R. Grindlay, J. A. Madsen, and C. Rommevaux-Jestin (2005). Tectonic interpretation of the Andrew Bain transform fault: Southwest Indian Ocean, *Geochem. Geophys. Geosys.* **6,** no. 9, doi: 10.1029/2005GC000951.

Sigmundsson, F., V. Pinel, R. Grapenthin, A. Hooper, S. A. Halldórsson, P. Einarsson, B. G. Ófeigsson, E. R. Heimisson, K. Jónsdóttir, M. T. Gudmundsson, *et al.* (2020). Unexpected large eruptions from buoyant magma bodies within viscoelastic crust, *Nat. Commun.* **11,** no. 1, doi: 10.1038/s41467-020-16054-6.

Stefánsson, R., G. B. Gudmundsson, and P. Halldórsson (2008). Tjornes fracture zone. New and old seismic evidences for the link between the North Iceland rift zone and the Mid-Atlantic ridge, *Tectonophysics* **447,** nos. 1/4, 117–126.

Styron, R. (2019). The impact of earthquake cycle variability on neotectonic and paleoseismic slip rate estimates, *Solid Earth* **10,** no. 1, 15–25.

Sykes, L. R., and G. Ekstrom (2012). Earthquakes along Eltanin transform system, SE Pacific Ocean: Fault segments characterized by strong and poor seismic coupling and implications for long-term earthquake prediction, *Geophys. J. Int.* **188,** no. 2, 421–434.

Thordarson, T., and A. Höskuldsson (2008). Postglacial volcanism in Iceland, *Jökull* **58,** 197–228.

Thordarson, T., and G. Larsen (2007). Volcanism in Iceland in historical time: Volcano types, eruption styles and eruptive history, *J. Geodynam.* **43,** no. 1, 118–152.

Thorgeirsson, O. (2011). Historical earthquakes in north Iceland (in Icelandic), *Husavik Academic Center*.

Tibaldi, A., F. L. Bonali, P. Einarsson, A. R. Hjartardóttir, and F. A. Mariotto Pasquare (2016). Partitioning of Holocene kinematics and interaction between the Theistareykir Fissure Swarm and the Husavik-Flatey Fault, North Iceland, *J. Struct. Geol.* **83,** 134–155.

van Loon, A. J., M. Pisarska Jamrozy, M. Nartiss, M. Krievans, and J. Soms (2016). Seismites resulting from high frequency, high magnitude earthquakes in Latvia caused by Late Glacial glacio-isostatic uplift, *J. Palaeogeogr.* **5,** no. 4, 363–380.

Vogt, P. R., G. L. Johnson, and L. Kristjansson (1980). Morphology and magnetic anomalies north of Iceland, *J. Geophys.* **47,** nos. 1/3, 67–80.

20 Waitt, R. B. (2002). *Great Holocene Floods Along J okulsa a Fj ollum, North Iceland*, John Wiley and Sons, Ltd., 37–51.

Waltl, P., B. Halldórsson, H. G. Petursson, and M. Fiebig (2018). Geomorphic assessment of the urban setting of Husavik, North Iceland, in the context of earthquake hazard, *Jokull* **68,** 27–46.

Wells, G. H., A. J. Dugmore, T. Beach, E. R. C. Baynes, T. Sæmundsson, and S. Beach-Luzzadder (2022). Reconstructing glacial outburst floods (Jökulhlaup) from geomorphology: Challenges, solutions, and an enhanced interpretive framework, *Prog. Phys. Geogr.* **46,** no. 3, 398–421.

Wendt, J. I., M. Regelous, Y. Niu, R. Hékinian, and K. D. Collerson (1999). Geochemistry of lavas from the Garrett Transform Fault: Insights into mantle heterogeneity beneath the eastern Pacific, *Earth Sci. Planet. Lett.* **173,** no. 3, 271–284.

Wheeler, R. L. (2002). Distinguishing seismic from nonseismic soft 21 sediment structures; criteria from seismic hazard analysis, in *Ancient Seismites*, Geological Society of America.

Wilson, J. T. (1965). A new class of faults and their bearing on continental drift, *Nature* **207,** 343–347.

Youd, T. L., and C. T. Garris (1995). Liquefaction-induced ground-surface disruption, *J. Geotech. Eng.* **121,** 11, 805–809.

Youd, T. L., and D. M. Perkins (1987). Mapping of liquefaction severity index, *J. Geotech. Eng.* **113,** no. 11, 1374–1392.

**Manuscript received 19 June 2023**

## Queries

1. AU: Please indicate if the roman capital M throughout the article should be changed to (1) bold **M** or (2) $M_w$ (italic "M" and subscript roman "w").
2. AU: Please provide a definition of "MORVEL"; it will be included before the abbreviation.
3. AU: This should be 8 or 9 instead of 8–9, as this has to be a certain number for earthquakes. Kindly verify.
4. AU: This should be three or four instead of three to four, as this has to be a certain number for earthquakes. Kindly verify.
5. AU: Kindly verify.
6. AU: According to SSA style, figures must be cited in numerical order within the article's text. Figure 10 is cited before Figure 9. Please review and edit as necessary by either (1) providing text locations in which mentions of Figure 9 may be inserted *before* the occurrence of the first mention of Figure 10, or (2) indicate that the figure numbers (and corresponding cross-references) should be renumbered throughout the article.
7. AU: Please provide page numbers for all direct quotes that are not electronically published.
8. AU: Five disturbances have been mentioned in contrast to the six listed disturbances "two on the Skjólbrekka fault (SK1 and SK3) and four on Laugardalur fault where our trench Tr1 is located (SK2–SK5)." This description is highly confusing. Kindly verify.
9. AU: SSA tries to avoid using a slash in nonmathematical contexts. Please provide alternative wording for "E6/E7."
10. AU: As per SSA style, the abbreviation "(GNSS)" has been deleted because it is not used again in this article.
11. AU: Please verify the URL (https://www.lmi); it is not accessible as currently written. Kindly provide valid URL and its last accessed month and year.
12. AU: Please provide a definition of "IMO"; it will be included before the abbreviation.
13. AU: BSSA has many associate editors; do you wish to name a specific one?
14. AU: For Brothers et al. (2020), please provide page range or doi number.
15. AU: For Heap et al. (2020), please provide page range or doi number.
16. AU: For reference Hey (2005) Please provide editor name, publisher name and publisher location.
17. AU: For reference Müller et al. (2021) Please provide location of the publisher.
18. AU: For Óladóttir et al. (2020), please provide page range or doi number.
19. AU: For Sæmundsson (2013), please provide location and date of the conference where and when was it held.
20. AU: For reference Waitt (2002) Please provide publisher location.
21. AU: For reference Wheeler (2002) Please provide editor name and publisher location.
22. AU: Please provide a definition of "ICEL-NMAR"; it will be included before the abbreviation.
23. AU: The citation "Jóasson et al. (2021)" does not have a corresponding Reference entry. There is a "Jónasson et al. (2021)" in the References, which is not cited in the paper. Please (1) decide whether these refer to the same work and (2) indicate the required changes to the paper and the References.
24. AU: Kindly verify the edited text for its intended meaning.
25. AU: Figure 6, please provide description for the figure present above panel (a).
26. AU: Figure 11, please provide description for the figure present above panel (a) to include in caption.
27. AU: Figure 12, please note that there are labels from a to e inside the figure. Please ckeck and provide revised figure if needed.
28. AU: Please provide a definition of "AMS"; it will be included before the abbreviation.
29. AU: Although "Stuiver and Polach, 1977" is cited, there is no corresponding Reference entry. Please provide a Reference entry for this citation, or indicate the citations should be deleted throughout the article.
30. AU: Although "Eiríksson et al., 2004" is cited, there is no corresponding Reference entry. Please provide a Reference entry for this citation, or indicate the citations should be deleted throughout the article.
31. AU: Although "Hartley et al., 2016" is cited, there is no corresponding Reference entry. Please provide a Reference entry for this citation, or indicate the citations should be deleted throughout the article.